Journal of Colloid and Interface Science 678 (2025) 804–818

Contents lists available at ScienceDirect

Journal of Colloid And Interface Science

journal homepage: www.elsevier.com/locate/jcis

In situ fabrication of Ni_3S_2/Cu_2S heterojunction on nickel foam as a highly efficient and durable electrocatalyst for overall water splitting

Siqi Zhang [a], Huiqin Yao [b,*], Ruxin Deng [a], Jiayi Zhan [a,1], Tian Tong [a,2], Yixuan Wang [a,3], Haiqing Yan [a], Chaonan Wang [a], Cheng Li [c,*], Hongliang Dong [d,e,*], Shulan Ma [a,*]

[a] Beijing Key Laboratory of Energy Conversion and Storage Materials and College of Chemistry, Beijing Normal University, Beijing 100875, China
[b] School of Basic Medical Sciences, Ningxia Medical University, Yinchuan 750004, China
[c] Shanghai Institute of Applied Physics, Chinese Academy of Sciences, Shanghai 201800, China
[d] Center for High Pressure Science and Technology Advanced Research, Shanghai 201203, China
[e] Shanghai Key Laboratory of Material Frontiers Research in Extreme Environments (MFree), Shanghai Advanced Research in Physical Sciences (SHARPS), Pudong, Shanghai 201203, China

HIGHLIGHTS

- NF/Ni_3S_2/Cu_2S heterojunction is fabricated via an electrodeposition-hydrothermal method.
- NF/Ni_3S_2/Cu_2S shows ultra-low overpotentials of 108 for HER and 166 mV for OER at 10 mA cm^{-2}.
- NF/Ni_3S_2/Cu_2S exhibits a much low cell voltage of 1.50 V for overall water splitting with long stability time (>150 h).
- The calculated DOS indicates Ni_3S_2/Cu_2S has a high carrier density at Fermi level.
- DFT calculations show interfacial effect of Ni_3S_2/Cu_2S weakens S—H bond and reduces $|\Delta G_{H^*}|$.

GRAPHICAL ABSTRACT

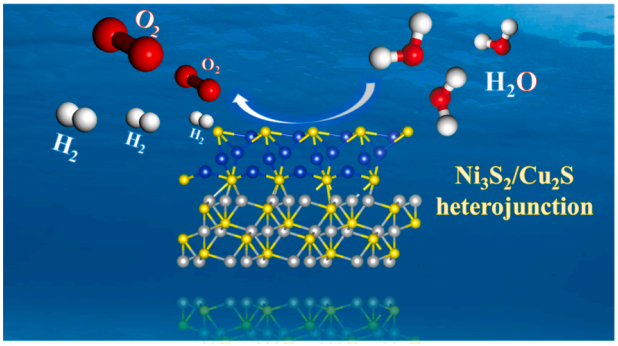

ARTICLE INFO

Keywords:
Hydrogen energy
Metallic sulfides
Heterojunction
Electrocatalysts
Overall water splitting

ABSTRACT

The development of cost-efficient bifunctional electrocatalysts is significant for overall water splitting. Herein, we report the in situ fabrication of heterogeneous NF/Ni_3S_2/Cu_2S-X (where X refers to Cu^{2+} concentrations of 50, 75, and 100 mM) on nickel foam (NF) using an electrodeposition–hydrothermal method. The in situ electrodeposited metallic Cu^0 layers on the NF conferred higher stability to the resulting bimetallic sulfide of Ni_3S_2/Cu_2S. In alkaline media (1 M KOH), the optimized NF/Ni_3S_2/Cu_2S-75 exhibited ultra-low overpotentials of 108 and 166 mV during the hydrogen evolution reaction (HER) and oxygen evolution reaction (OER) at 10 mA·cm^{-2}. For overall water splitting, the catalyst showed a significantly low cell voltage of 1.50 V and long stabilization time (≥150 h) at 15 mA·cm^{-2}. Density functional theory calculations revealed that the formation of Ni_3S_2/Cu_2S heterojunction reduced the Gibbs free energy of hydrogen adsorption (ΔG_{H^*}) on the S site, thus facilitating H_2

* Corresponding authors.
E-mail addresses: huiqin_yao@163.com (H. Yao), licheng@sinap.ac.cn (C. Li), hongliang.dong@hpstar.ac.cn (H. Dong), mashulan@bnu.edu.cn (S. Ma).
[1] Present address: The British School of Beijing, Shunyi, Beijing 101300, China.
[2] Present address: Capital Normal University high school, Beijing 100048, China.
[3] Present address: Beijing No.4 High School, Beijing 100031, China.

https://doi.org/10.1016/j.jcis.2024.09.110
Received 2 July 2024; Received in revised form 10 September 2024; Accepted 11 September 2024
Available online 14 September 2024
0021-9797/© 2024 Elsevier Inc. All rights are reserved, including those for text and data mining, AI training, and similar technologies.

generation. This study serves as a guide for tailoring transition metal-based catalysts with enhanced activity and long-term durability, thereby contributing to highly efficient water electrolysis for large-scale hydrogen production.

1. Introduction

The excessive utilization of fossil resources has resulted in severe energy crises and environmental pollution. Therefore, the development of fossil-free, cost-effective renewable energy sources is urgently needed. Hydrogen energy, owing to its advantages of zero pollution and high energy density (122 KJ g^{-1}) [1], is considered a promising alternative. Current techniques for water splitting encompass electrocatalytic and photocatalytic water splitting [2]. Electrocatalytic water splitting is the most widely used method for hydrogen production. However, it typically requires high overpotentials for the efficient anodic oxygen evolution reaction (OER) and cathodic hydrogen evolution reaction (HER) [3]. The OER involves a four-electron reaction and thus has slow kinetics [4,5]. Ru/Ir oxides and Pt-based materials have been recognized as effective electrocatalysts; however, their high cost and limited stability hinder their large-scale utilization [6,7]. In addition, most materials catalyze only one half-reaction (OER or HER). Therefore, cost-effective bifunctional electrocatalysts with favorable OER and HER activities must be explored.

Transition metal-based catalysts, such as oxides [8], hydroxides [9], sulfides [10], and selenides [11], have garnered significant attention. Among these, sulfides have emerged as promising electrocatalysts for water splitting owing to their natural abundance [12–14]. Cu_2S has demonstrated good catalytic performance for overall water splitting [15,16]. However, the Cu_2S alone shows unsatisfactory stability. Marimuthu et al. [17] prepared Cu_2S supported on nickel foam (NF) via a low-temperature hydrothermal method, and the Cu_2S sample prepared at 80 °C showed the OER and HER overpotentials of 268 and 141 mV, respectively, at 10 mA cm^{-2} (the overpotential at 10 mA cm^{-2} is named as η_{10}). Despite the acceptable activity, its stability was limited to 10 h. Therefore, the stability of Cu_2S was improved by forming heterojunctions with other suitable components [15,18–20]. For example, Hu et al. [15] prepared Cu_2S/FeOOH on Cu foam (CF) via a calcination–hydrothermal reaction, achieving relatively longer stability for 36 h and low η_{10} values of 136 mV for HER and 208 mV for OER. In another study, Zang et al. [20] synthesized Co_9S_8/Cu_2S/CF by electrodepositing $Cu(OH)_2$ on CF, followed by sulfidation, which exhibited low η_{10} of 195 mV for OER and 165 mV for HER, with stability time exceeding 24 h. Density functional theory (DFT) calculations substantiated that interfacial interactions enhanced the adsorption of oxygen-containing intermediates and dissociation of water molecules.

Nickel sulfides, such as NiS [21], NiS_2 [22], Ni_3S_2 [23], Ni_3S_4 [24], and Ni_9S_8 [25], have received considerable attention because of the diverse valences of Ni/S arising from their multiple compositions. Notably, Ni_3S_2 has an Ni–Ni interconnected network, high metallic conductivity, and strong corrosion resistance [6,26], making it suitable for constructing hybrid electrocatalysts with enhanced OER and HER performance [27,28].

In this study, we fabricated an Ni_3S_2/Cu_2S heterojunction grown in situ on NF via a facile electrodeposition–hydrothermal method. Compared with previous studies synthesizing Cu_2S on CF [15,20], this study employed electrodeposition to uniformly deposit pure metallic Cu layers on the NF, which were subsequently vulcanized to form metal sulfides. The NF not only serves as a three-dimensional (3D) substrate to enhance the surface area and ion transfer [29], but also as an Ni source to generate various nickel sulfides via vulcanization [30–32]. This novel approach results in a more compact structure of the catalyst with better contact with the NF substrate, thereby enhancing catalytic stability. The electrocatalytic activity and durability of the NF/Ni_3S_2/Cu_2S outperform most other state-of-the-art electrocatalysts. DFT calculations demonstrate the good electrical conductivity and electrocatalytic activity, as evidenced by the density of state (DOS), Gibbs free energy of hydrogen adsorption (ΔG_{H^*}), and charge differential density. Thus, NF/Ni_3S_2/Cu_2S is a promising electrocatalyst for large-scale hydrogen production.

2. Materials and methods

2.1. Chemicals and materials

The following chemicals and materials were used in this study: $Cu(NO_3)_2{\cdot}3H_2O$ (Tianjin Damao Chemical Reagent Co., Ltd., 99.5%), $(NH_4)_6Mo_7O_{24}{\cdot}4H_2O$ (Bide Pharmatech Co., Ltd., 99.0%), thiourea (CH_4N_2S, Tianjin Dingshengxin Chemical Reagent Co., Ltd., 99.0%), nickel foam (Shenzhen Tianchenghe Technology Co. Ltd.), KOH (Beijing Chemical Reagent Co., Ltd., 82.0%), and Cu_2S (Macklin Chemical Reagent Co., Ltd., 99%).

2.2. Characterizations

The samples structures were analyzed using an X'pert pro MPD diffractometer (Cu Kα radiation, λ = 1.54056 Å), operating at 40 kV and 40 mA. The morphologies of the samples were examined using field-emission scanning electron microscopy (FE-SEM; SU-8010, Hitachi) at an acceleration voltage of 10 kV and high-resolution transmission electron microscopy (HRTEM; JEM-2010, JEOL, and FEI Technai G2 F20) at 200 kV. The specific surface areas of the samples were calculated using the Brunauer–Emmett–Teller (BET) method, and the pore sizes and volumes were calculated using the Barrett–Joyner–Halenda (BJH) method. X-ray photoelectron spectroscopy (XPS) spectra were obtained using an ESCALAB 250Xi spectrometer (Thermo Fisher) with Al-Kα radiation. Inductively coupled plasma-atomic emission spectroscopy (ICP-AES; Jarrel-ASH, ICAP-9000) was used to determine the Ni, Cu and Mo contents in the samples, which were first dissolved in aqua regia.

2.3. Synthesis of electrocatalysts

First, three pieces of NF (area was 1 × 2 cm^2) were ultrasonically treated with 1.0 M hydrochloric acid to eliminate the oxide layer on the NF surface, then ultrasonically cleaned with acetone, deionized water, and ethanol, and finally vacuum-dried.

NF/Cu-X (where X refers to the Cu^{2+} concentrations of 50, 75, and 100 mM) was synthesized via electrodeposition using a CHI600 electrochemical workstation. The NF (the area immersed in solution was 1 × 1 cm^2), saturated calomel electrode (SCE), and a platinum plate were used as working, reference, and counter electrodes, respectively. Taking NF/Cu-75 as an example, NF was electrodeposited for 10 min in a 75 mM $Cu(NO_3)_2$ aqueous solution at −1.0 V *vs.* SCE. After washing with water and ethanol and vacuum drying for 12 h, NF/Cu-75 was obtained.

NF/Ni_3S_2/Cu_2S-X samples were prepared using a hydrothermal method. Taking NF/Ni_3S_2/Cu_2S-75 as an example, three pieces of NF/Cu-75 were added to a 50 mL Teflon-lined stainless steel autoclave containing 30 mL of aqueous solution of thiourea (CH_4N_2S, 2 mmol) and ammonium molybdate tetrahydrate ($(NH_4)_6Mo_7O_{24}{\cdot}4H_2O$, 0.08 mmol). Subsequently, the autoclave was sealed and heated in an oven at 200 °C for 12 h. After cooling to 25 °C, the sample was washed with deionized water and ethanol and vacuum-dried to obtain NF/Ni_3S_2/Cu_2S-75.

The control sample, NF/Ni_3S_2, was synthesized via a hydrothermal method using pure NF (1 × 2 cm^2) as a precursor instead of NF/Cu-75, with all other procedures similar to those used for NF/Ni_3S_2/Cu_2S-X.

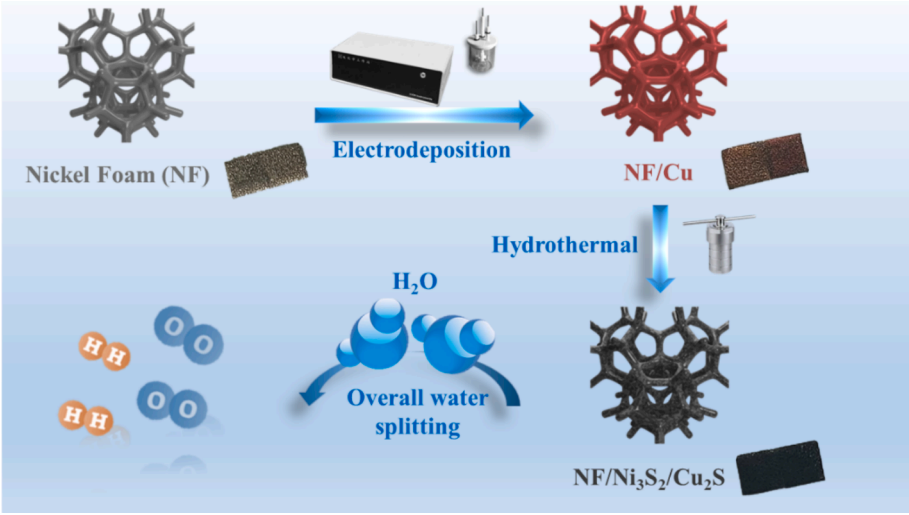

Scheme 1. Schematic illustration for the preparation of NF/Ni_3S_2/Cu_2S electrocatalyst.

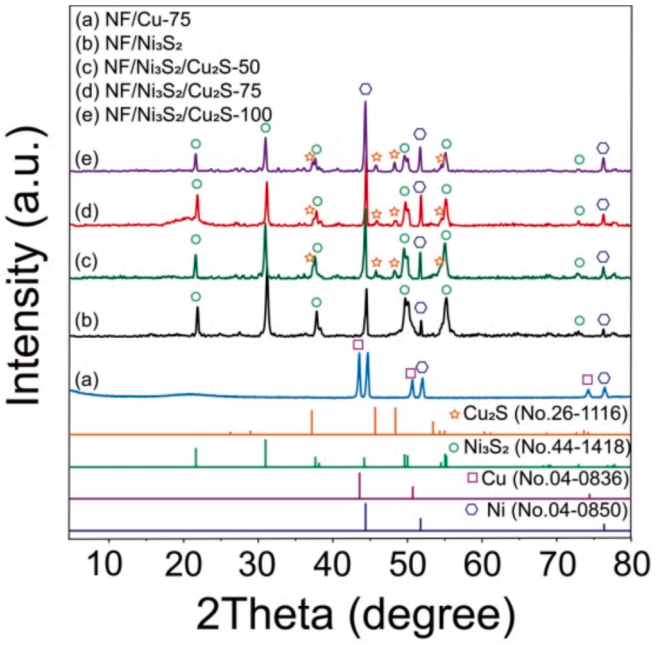

Fig. 1. XRD patterns of (a) NF/Cu-75, (b) NF/Ni_3S_2, (c) NF/Ni_3S_2/Cu_2S-50, (d) NF/Ni_3S_2/Cu_2S-75, and (e) NF/Ni_3S_2/Cu_2S-100.

The amounts of the starting materials and the mass loadings of the resulting samples on NF are listed in Table S1 and S2, respectively.

2.4. X-ray absorption near edge structure (XANES) measurements

The Ni K-edge (8333 eV) and Cu K-edge (8979 eV) XANES spectra were recorded in the fluorescence mode at the BL14W1 beamline station of the Shanghai Synchrotron Radiation Facility. Self-absorption effects were corrected prior to analysis. Photon energies were calibrated to the first inflection point of the Ni K-edge in the Ni foil and the Cu K-edge in the Cu foil. All the data were processed using the ATHENA and ARTEMIS programs in the Demeter package, and the theoretical backscattering phase was calculated using FEFF 8.2 code [33].

2.5. DFT calculations

DFT calculations were performed to determine the HER and OER activities of Ni_3S_2/Cu_2S using the Vienna Ab initio simulation package [34]. Electron–ion interactions were described using projector-augmented-wave methods [35]. The exchange and correlation energies were calculated using the Perdew–Burke–Ernzerhof generalized gradient approximation. A cutoff kinetic energy of 400 eV was used for all the calculations, with a k-point mesh of 1 × 1 × 1 for the Brillouin zone. For lattice matching, the (0 0 1) planes of the 4 × 4 × 1 Cu_2S and 3 × 3 × 1 Ni_3S_2 cells were the optimal interfaces. To avoid vertical interactions, a vacuum layer of 15 Å was added in the *z*-direction. The structural models of Cu_2S and Ni_3S_2/Cu_2S were created to simulate the catalyst. Supplementary Note 1 lists the equations used in these calculations.

3. Results and discussions

3.1. Structural characterizations

Scheme 1 shows the synthesis of the NF/Ni_3S_2/Cu_2S via an electrodeposition–hydrothermal method. The aqueous solution contained two types of cations, Cu^{2+} and H^+. First, Cu^{2+} preferentially obtained electrons to form Cu metals **(Reaction 1)**, which was electrodeposited on the NF (labeled NF/Cu-X), changing its color to reddish-brown. The second step involved a hydrothermal process in which NH_2CSNH_2 provided S atoms, and $(NH_4)_6Mo_7O_{24}$ adjusted the sample morphology [36]. Ni_3S_2 was formed via two reactions: NH_2CSNH_2 disintegrated to release HS^- **(Reaction 2)**, and Ni^{2+} ions from the NF reacted with HS^- to form Ni_3S_2 **(Reaction 3)** [30,31,37]. During this process, the sample darkened. Cu^0 was oxidized to Cu^+ by HS^- released from NH_2CSNH_2 [30,31,37], and owing to the smaller solubility constant (K_{sp}) of Cu_2S ($K_{sp} = 2.5 \times 10^{-48}$ [38]) than that of CuS ($K_{sp} = 6.3 \times 10^{-36}$ [39]), Cu_2S was preferentially formed **(Reaction 4)**.

Step I (electrodeposition):

$$Cu^{2+} + 2e^- \rightarrow Cu \quad \text{(Reaction 1)}$$

Step II (hydrothermal reaction):

$$NH_2CSNH_2 + 3H_2O \rightarrow 2NH_4^+ + HS^- + HCO_3^- \quad \text{(Reaction 2)}$$

$$3Ni + 2HS^- + 2H_2O \rightarrow Ni_3S_2 + 2OH^- + 2H_2 \quad \text{(Reaction 3)}$$

$$2Cu + HS^- + H_2O \rightarrow Cu_2S + OH^- + H_2 \quad \text{(Reaction 4)}$$

Considering that $(NH_4)_6Mo_7O_{24}{\cdot}4H_2O$ was also added in the reaction, confirming the presence of Mo element in the product was important. ICP-AES was performed to quantify the Ni, Cu and Mo

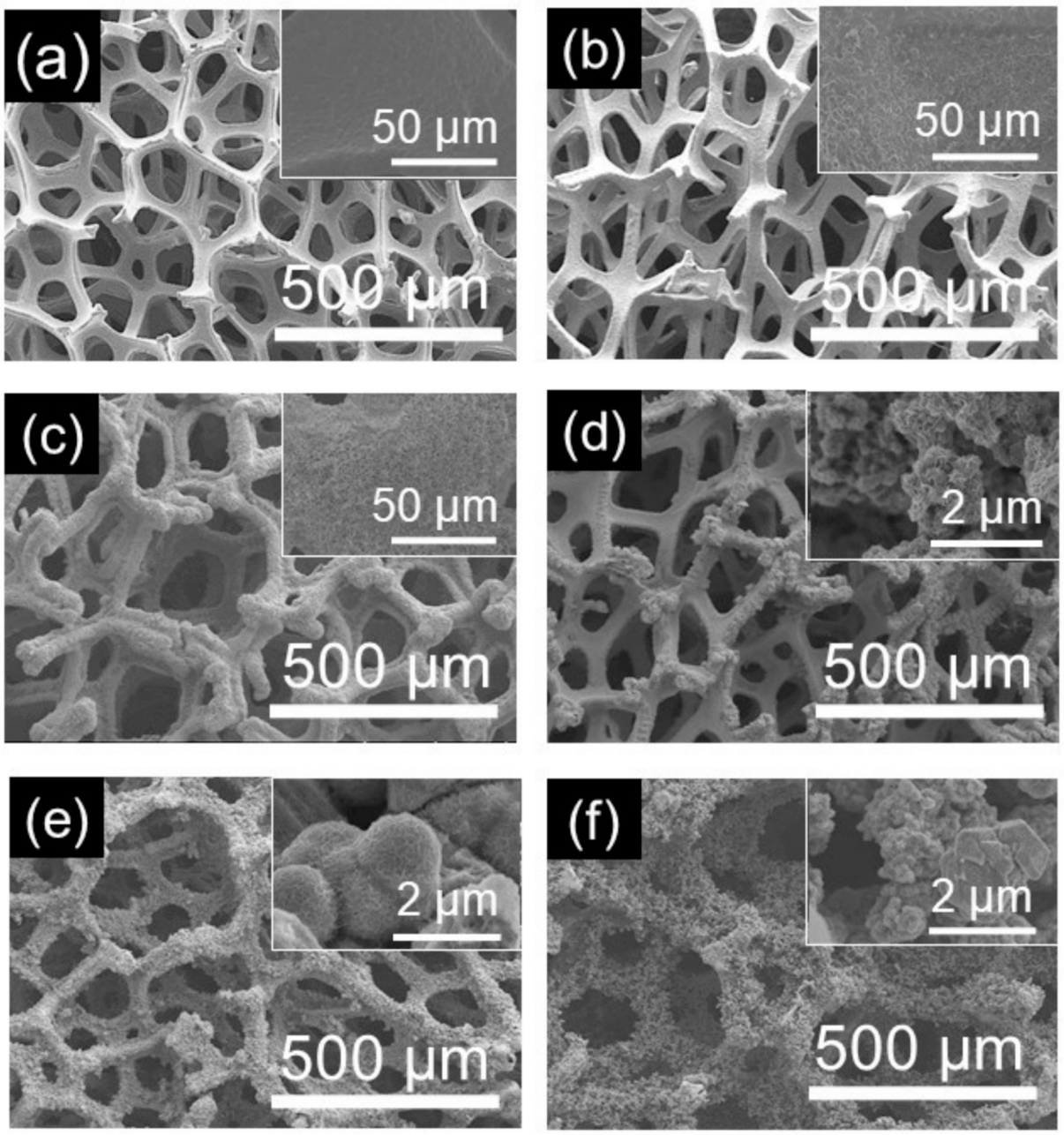

Fig. 2. SEM images of (a) NF, (b) NF/Cu-75, (c) NF/Ni_3S_2, (d) NF/Ni_3S_2/Cu_2S-50, (e) NF/Ni_3S_2/Cu_2S-75, and (f) NF/Ni_3S_2/Cu_2S-100 at different magnifications.

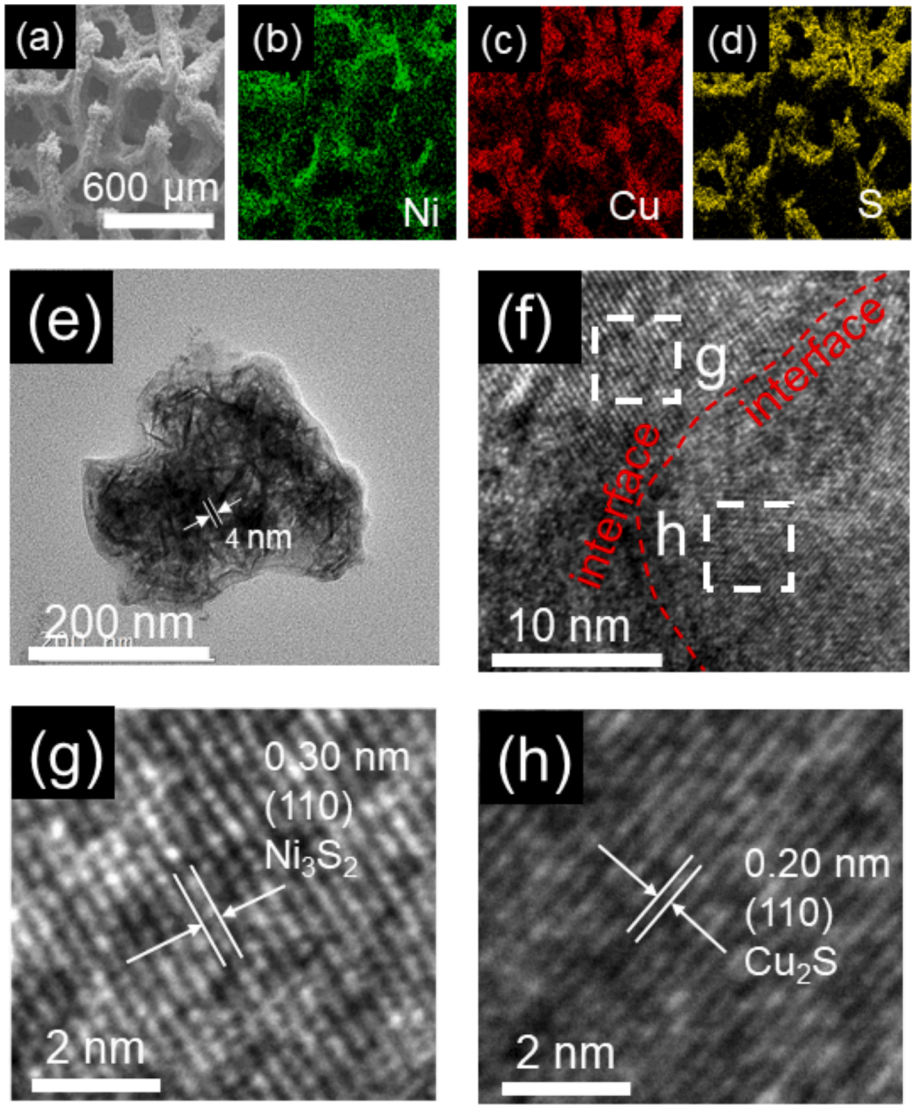

Fig. 3. (a) SEM image of NF/Ni_3S_2/Cu_2S-75 and (b-d) SEM-EDS elemental mapping of Ni, Cu, and S in the image of (a). (e) TEM image and (f) HR-TEM image of NF/Ni_3S_2/Cu_2S-75, (g, h) are enlarged HRTEM images of the selected area in (f).

contents. Before the ICP tests, the solid samples were dissolved in aqua regia. Because S reacted with aqua regia to release H_2S gas, the exact content of S in the solid samples could not be determined; therefore, we only obtained the Ni, Cu, and Mo contents (wt%), which were 67.4%, 12.6%, and 0.017%, respectively. The extremely low Mo content (< 0.05%) suggested the absence of Mo-based compounds such as MoS_2. Additionally, the Ni:Cu molar ratio of 5.8:1 indicates a high proportion of Ni, primarily originating from the NF.

XRD analysis was performed to explore the structures and compositions of NF/Cu-75, NF/Ni_3S_2, NF/Ni_3S_2/Cu_2S-50, NF/Ni_3S_2/Cu_2S-75, and NF/Ni_3S_2/Cu_2S-100. The strong peaks at 44.5°, 51.8°, and 76.4° in all the sample spectra suggest the presence of metallic Ni^0 (JCPDS No. 04–0850) [40], derived from the NF. In the NF/Cu-75 spectra (Fig. 1a), the peaks at 43.3°, 50.4°, and 74.1° matched well those of metallic Cu (JCPDS No. 04–0836) [41], indicating the formation of NF/Cu. In the NF/Ni_3S_2 spectra (Fig. 1b), the peaks at 21.7°, 31.1°, 37.8°, 50.1°, 55.2°, and 73.0° correspond to the (101), (110), (003), (211), (122), and (214) crystal planes of Ni_3S_2 (JCPDS No. 44–1418) [42]. In the NF/Ni_3S_2/Cu_2S-X spectra (Fig. 1c–e), in addition to the diffraction peaks of NF and Ni_3S_2, the peaks at 37.4°, 45.8°, 48.4°, and 54.6° corresponding to the (102), (110), (103), and (004) planes of Cu_2S were observed (JCPDS No. 26–1116) [15], suggesting the successful synthesis of NF/Ni_3S_2/Cu_2S.

The morphologies of the NF, NF/Cu-75, NF/Ni_3S_2, and NF/Ni_3S_2/Cu_2S-X were analyzed using SEM. The bare NF had a porous 3D network with a smooth surface (Fig. 2a). After metallic Cu grew on the NF surface (NF/Cu-75, see Fig. 2b), the porous morphology was maintained; however, the surface was covered by numerous particles. The control sample, NF/Ni_3S_2, had many interlaced sheets that grew on the NF (Fig. 2c). NF/Ni_3S_2/Cu_2S-75 grew uniformly on the NF (Fig. 2e), and the magnified image shows sheets interlaced with a regular micron spheroidal morphology. However, at a Cu^{2+} concentration of 50 mM (Fig. 2d), the mass loading was lower and the sheets did not grow completely on the NF surface, whereas at a Cu^{2+} concentration of 100 mM (Fig. 2f), the NF skeleton loosened and many irregular bulks were formed on the surface because of excessive loading. The NF/Ni_3S_2/Cu_2S-75 possessed the largest specific surface area, facilitating contact with the electrolyte. Scanning electron microscope-energy dispersive spectrometry (SEM-EDS) elemental mappings (Fig. 3a–d) demonstrated the uniform distribution of Ni, Cu, and S elements in NF/Ni_3S_2/Cu_2S-75. Thus, the morphology of the sulfides can be optimized by tuning the Cu^{2+} dosage to achieve superior electrocatalytic performance, as discussed below.

The BET specific surface areas (S_{BET}) and pore characteristics of NF/Ni_3S_2/Cu_2S-75 and NF/Ni_3S_2/Cu_2S-50 were determined using N_2

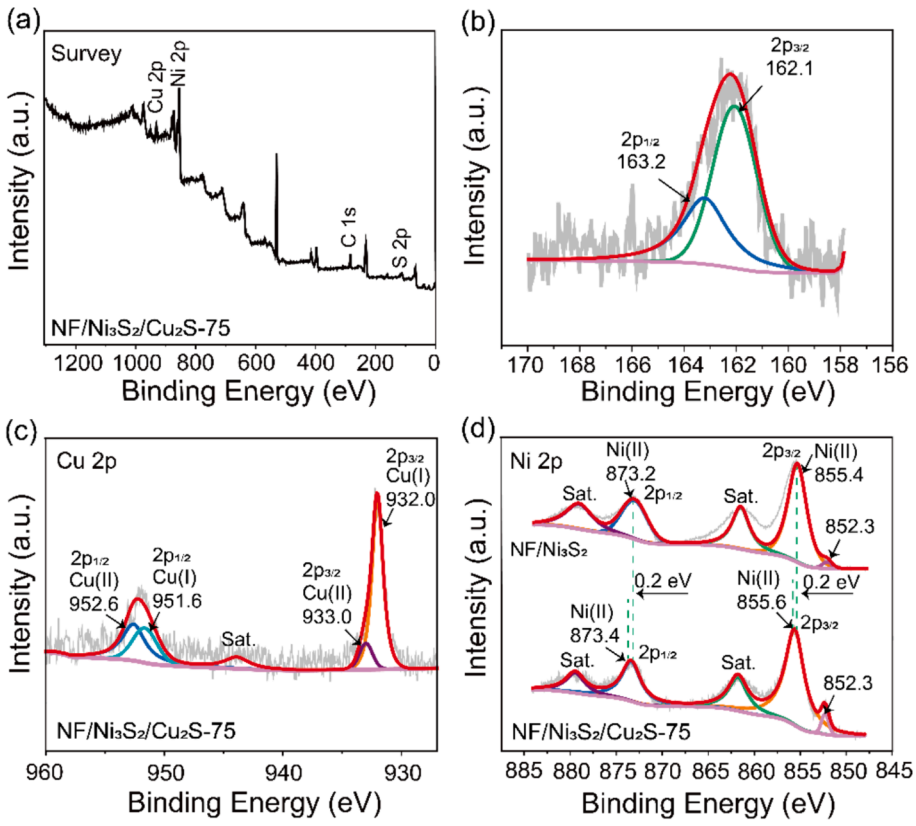

Fig. 4. XPS spectra: (a) survey spectrum, (b) S 2p, and (c) Cu 2p of NF/Ni_3S_2/Cu_2S-75, and (d) Ni 2p of NF/Ni_3S_2 and NF/Ni_3S_2/Cu_2S-75.

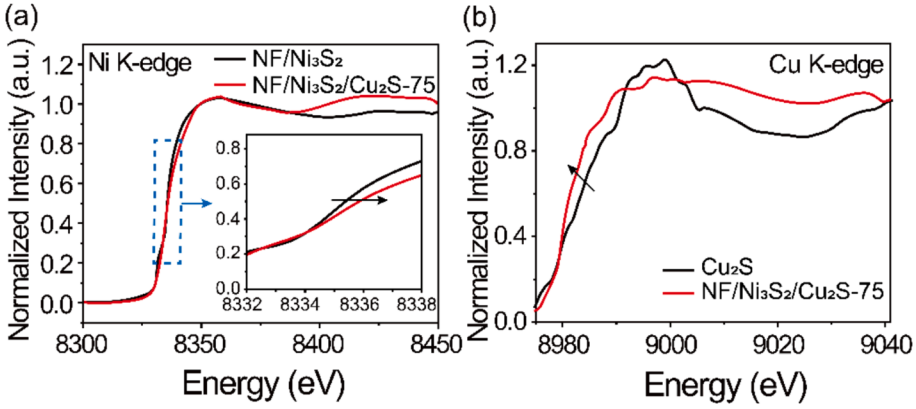

Fig. 5. XANES spectra of (a) Ni K-edge of NF/Ni_3S_2 and NF/Ni_3S_2/Cu_2S-75, (b) Cu K-edge of Cu_2S and NF/Ni_3S_2/Cu_2S-75.

sorption measurements. As depicted in Fig. S1, the S_{BET} of NF/Ni_3S_2/Cu_2S-75 and NF/Ni_3S_2/Cu_2S-50 were 10.8 and 6.8 m^2/g, respectively, with pore sizes of approximately 3.8 nm. These results demonstrate that, although their pore sizes were similar, the specific surface area of NF/Ni_3S_2/Cu_2S-75 was twice that of NF/Ni_3S_2/Cu_2S-50, which is consistent with the SEM observations.

The XRD pattern of NF/Ni_3S_2/Cu_2S-C (Fig. S2A-a) was similar to that of NF/Ni_3S_2/Cu_2S-75 (Fig. S2A-b). However, the SEM images (Fig. S2B-a) indicated that NF/Ni_3S_2/Cu_2S-C exhibited an irregular morphology and low mass loading. This suggests that $(NH_4)_6Mo_7O_{24}{\cdot}4H_2O$ plays an indispensable role in the formation of micron spheroidal structure.

TEM observations further verified the structure and morphology of the samples. For the TEM measurements, the Ni_3S_2/Cu_2S sample was peeled off the NF surface via intensive sonication. Fig. 3e shows a nanosheet structure (~4 nm thick) on the NF/Ni_3S_2/Cu_2S-75 surface. The HRTEM image (Fig. 3f) reveals an interface between Ni_3S_2 and Cu_2S. The images (Fig. 3g, h) of the selected regions of Fig. 3f show two sets of lattice fringe spacings of 0.30 and 0.20 nm, corresponding to the (1 1 0) planes of Ni_3S_2 [43] and Cu_2S [44], respectively, which are consistent with the XRD results. These results confirm the formation of a Ni_3S_2/Cu_2S heterojunction.

3.2. Electronic state characterization

XPS was used to investigate the chemical states of the elements. The full survey spectrum of NF/Ni_3S_2/Cu_2S-75 showed the presence of Cu, Ni, and S elements (Fig. 4a). In the S 2p spectra (Fig. 4b), the peaks at 162.1 and 163.2 eV corresponded to the $2p_{3/2}$ and $2p_{1/2}$ states of S^{2-} [45]. The Cu 2p spectra (Fig. 4c) showed two peaks at 932.0 and 951.6 eV, corresponding to the $2p_{3/2}$ and $2p_{1/2}$ states of Cu^+ [46,47], and two

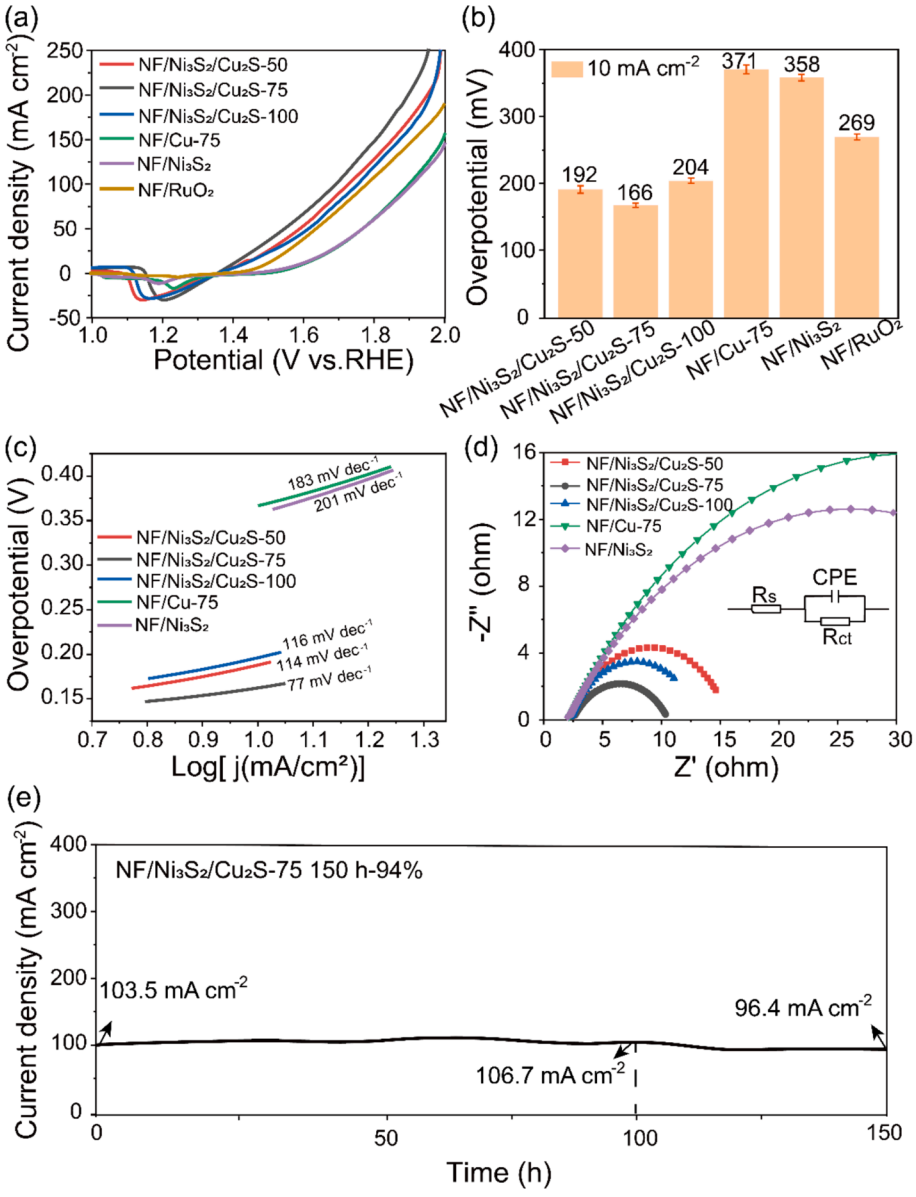

Fig. 6. OER performance of NF/Ni_3S_2/Cu_2S-X, NF/Cu-75, NF/Ni_3S_2, and NF/RuO_2 in 1 M KOH. (a) LSV curves for all samples (no iR correction). (b) The overpotentials of all samples at 10 mA cm^{-2}. The measured data were obtained at least after three times experiments. (c) Tafel plots of NF/Ni_3S_2/Cu_2S-X, NF/Cu-75, and NF/Ni_3S_2. (d) Nyquist plots of NF/Ni_3S_2/Cu_2S-X, NF/Cu-75, and NF/Ni_3S_2. (e) Chronoamperometric curve of NF/Ni_3S_2/Cu_2S-75 at a constant applied potential of 1.73 V *vs* RHE.

Table 1
Electrocatalytic performance of NF/Ni_3S_2/Cu_2S-75 with other reported electrocatalysts in 1 M KOH.

Catalysts	η_{10} (mV)		Overall water splitting (10 mA cm^{-2})		References
	OER	HER	Cell voltage (V)	Stability time (h)	
NF/Ni_3S_2/Cu_2S-75	**166**	**108**	**1.50**	**150**[a]	**This work**
$MoSe_2$-Cu_2S NHSs	264	350	–	–	J. Mater. Chem. A. 2021. [58]
Cu_2S NRs@CoS/CF	208	136	–	–	Electrochim. Acta 2019. [59]
Cu_2S-Ni_3S_2/NF	329	149	1.77	100[b]	Chem. Select. 2020. [18]
Co_9S_8/Cu_2S/CF	195	165	1.60	8	ACS Appl. Mater. Inter. 2021. [20]
Cu_2S@NF	194	105	1.64	20	Int. J. Hydrogen Energ. 2022. [61]
Cd-Ni_3S_2/NF-1/4	197	140	1.54	50	J. Alloy. Compd. 2023. [23]
MoS_2/Ni_3S_2	218	110	1.56	10	Angew. Chem. Int. Ed. 2016. [62]
Co_9S_8/Ni_3S_2	227	128	1.64	12	Appl. Catal. B: Environ. 2019. [60]
Ni_3S_2/$NiMo_2S_4$-POM/NF	136	126	1.53	20[c]	J. Alloys Compd. 2023. [63]
$Mo_{(1-x)}W_xS_2$@Ni_3S_2	285	98	1.62	50	ACS Appl. Mater. Inter. 2017. [64]
FeS/Ni_3S_2@NF	192	130	1.51	50	J. Colloid Interf. Sci. 2022. [65]
Ni_3S_2/$FeNi_2S_4$	201	50	1.55	50[d]	Chem. Eng. J. 2022. [28]

[a] the current density is 15 mA cm^{-2}.
[b, c] the current density is 20 mA cm^{-2}.
[d] the current density is 100 mA cm^{-2}.

peaks at 933.0 and 952.6 eV, corresponding to the $2p_{3/2}$ and $2p_{1/2}$ states of Cu^{2+} [48,49]. This indicates co-existence of Cu^+ and Cu^{2+} in NF/Ni_3S_2/Cu_2S-75. The presence of Cu^+ confirmed the formation of Cu_2S, and a small amount of Cu^{2+} was produced by the oxidation of the Cu_2S surface when exposed to air [38]. In the NF/Ni_3S_2/Cu_2S-75 spectra, the two strong peaks at 855.6 and 873.4 eV (Fig. 4d) corresponded to Ni^{2+} $2p_{3/2}$ and $2p_{1/2}$ states [50]. The binding energy of 852.3 eV was related to Ni^0 of Ni_3S_2 and NF [51]. Satellite peaks were observed at 861.7 and 879.4 eV [52]. Compared with NF/Ni_3S_2, the Ni 2p binding energy for NF/Ni_3S_2/Cu_2S-75 shifted by +0.2 eV, indicating electron transfer between Ni_3S_2 and Cu_2S at the interface.

The electronic interactions between Ni_3S_2 and Cu_2S were further studied using XANES spectroscopy. Commercial Cu_2S was used as the control sample. Fig. 5a shows the Ni K-edge XANES spectra of NF/Ni_3S_2 and NF/Ni_3S_2/Cu_2S-75. The Ni K-edge in NF/Ni_3S_2/Cu_2S-75 shifted to a higher energy than in NF/Ni_3S_2, suggesting a higher valence of Ni [53] in NF/Ni_3S_2/Cu_2S-75. Fig. 5b shows the Cu K-edge spectra of Cu_2S and NF/Ni_3S_2/Cu_2S-75. The Cu K-edge in NF/Ni_3S_2/Cu_2S-75 shifted to a lower energy than in Cu_2S. In addition, compared with Cu_2S, the lower intensity of the white-line peak of Cu in NF/Ni_3S_2/Cu_2S-75 indicates a lower valence state of Cu. These results are consistent with XPS, confirming the electron transfer from Ni to Cu in NF/Ni_3S_2/Cu_2S-75. According to previous studies [54,55], the e_g orbital occupancy significantly influences the electrocatalytic performance of 3d transition metals, and the optimal e_g filling is approximately 1.2. The 3d-e_g orbitals form σ-bonds with the adsorbed oxygen during OER, owing to the strong overlapping between the 3d-e_g orbitals of transition metal ions and O 2p orbitals [54]. During OER, an electrocatalyst with a significantly high or low e_g occupancy (2 or 0) exhibits significantly strong or weak binding to O-related adsorbates, respectively, leading to unsatisfactory performance [56]. The initial electron configuration of Ni^{2+} was $t_{2g}^6e_g^2$, whereas after electron transfer, the electron configuration was close to the optimal e_g filling of 1.2, which is conducive to the improving the OER activity [55]. In terms of HER, Ni^{3+}-rich configurations can lower the $|\Delta G_{H^*}|$ [57].

3.3. Electrocatalytic OER performance

Using a standard three-electrode system, the electrochemical measurements were performed at 25 °C in 1 M KOH. Supplementary Note 2 provides the details of the measurements. As evident from linear sweep voltammetry (LSV) curves (Fig. 6a and b), the η_{10} for NF/Ni_3S_2/Cu_2S-75 (166 mV) was significantly lower than that for NF/Cu-75 (371 mV) and NF/Ni_3S_2 (358 mV), indicating significantly enhanced performance after the formation of the Ni_3S_2/Cu_2S heterojunction. Moreover, various Cu dosages exhibited different catalytic activities. The NF/Ni_3S_2/Cu_2S-75 exhibited the lowest η_{10} compared with NF/Ni_3S_2/Cu_2S-50 (192 mV) and NF/Ni_3S_2/Cu_2S-100 (204 mV), demonstrating its highest OER activity. Meanwhile, the control sample NF/Ni_3S_2/Cu_2S-C (synthesized without $(NH_4)_6Mo_7O_{24}{\cdot}4H_2O$), with its irregular morphology, resulted in a high overpotential of 231 mV compared with NF/Ni_3S_2/Cu_2S-X (X = 50, 75, and 100). The microspherical morphology of NF/Ni_3S_2/Cu_2S-75 provided abundant active sites and a large specific surface area, resulting in its superior performance. Table 1 compares the OER performance of NF/Ni_3S_2/Cu_2S-75 with other previously reported Ni_3S_2- and/or Cu_2S-based electrocatalysts [18,20,23,28,58–65]. The required overpotential of NF/Ni_3S_2/Cu_2S-75 (η_{10} = 166 mV) was found to be significantly lower than those of other Cu_2S-based electrocatalysts, such as Cu_2S@NF (194 mV) [61], Co_9S_8/Cu_2S/CF (195 mV) [20], and $MoSe_2$-Cu_2S NHSs (264 mV) [58]. This indicates that incorporating Ni_3S_2 into NF/Ni_3S_2/Cu_2S is beneficial for improving OER activity.

The Tafel slopes derived from the LSV curves reveal the reaction kinetics. The Tafel slope (b) was calculated using the equation η = b log (j) + a (where j: current density, a: constant, and η: overpotential) [66]. As shown in Fig. 6c, NF/Ni_3S_2/Cu_2S-75 exhibited a significantly lower Tafel slope (77 mV dec^{-1}) than NF/Ni_3S_2/Cu_2S-50 (114 mV dec^{-1}), NF/Ni_3S_2/Cu_2S-100 (116 mV dec^{-1}), NF/Cu-75 (183 mV dec^{-1}), and NF/Ni_3S_2 (201 mV dec^{-1}). This suggests that NF/Ni_3S_2/Cu_2S-75 exhibited the fastest reaction kinetics because of the interactions between Ni_3S_2 and Cu_2S [67].

The charge-transfer rate of the OER was studied using electrochemical impedance spectroscopy (EIS). As shown in Fig. 6d and Table S3, compared with other electrocatalysts, NF/Ni_3S_2/Cu_2S-75 exhibited the smallest charge-transfer resistance (R_{ct} = 8.2 Ω), implying the fastest charge transfer between the active sites on the NF/Ni_3S_2/Cu_2S-75 surface and the electrolyte.

Durability is a crucial criterion for practical applications of electrocatalysts, particularly at high current densities [68]. Fig. 6e shows the chronoamperometry test results of NF/Ni_3S_2/Cu_2S-75 at 100 mA cm^{-2}. Remarkably, no obvious attenuation in the current density was observed over 100 h, with only a 6% decay after 150 h, which demonstrates the excellent catalytic stability of NF/Ni_3S_2/Cu_2S-75 under alkaline conditions.

3.4. Electrocatalytic HER performance

The HER performance of NF/Ni_3S_2/Cu_2S-X, NF/Cu-75, NF/Ni_3S_2, and commercial 20 wt% Pt/C (on NF) was evaluated. As shown in Fig. 7a, NF/Ni_3S_2/Cu_2S-75 exhibited the lowest η_{10} (108 mV) compared with NF/Ni_3S_2/Cu_2S-50 (133 mV), NF/Ni_3S_2/Cu_2S-100 (115 mV), NF/Cu-75 (167 mV), and NF/Ni_3S_2 (139 mV). This confirms that the heterojunction between Ni_3S_2 and Cu_2S significantly enhanced the HER activity of NF/Ni_3S_2/Cu_2S-75. Additionally, an appropriate Cu dosage resulted in the formation of microspheres with sufficient active sites, thus enhancing the HER activity of NF/Ni_3S_2/Cu_2S-75. Moreover, Fig. S3c, d show that NF/Ni_3S_2/Cu_2S-75 (η_{10} = 108 mV) outperformed NF/Ni_3S_2/Cu_2S-C (138 mV). Fig. 7b provides a comparison of the

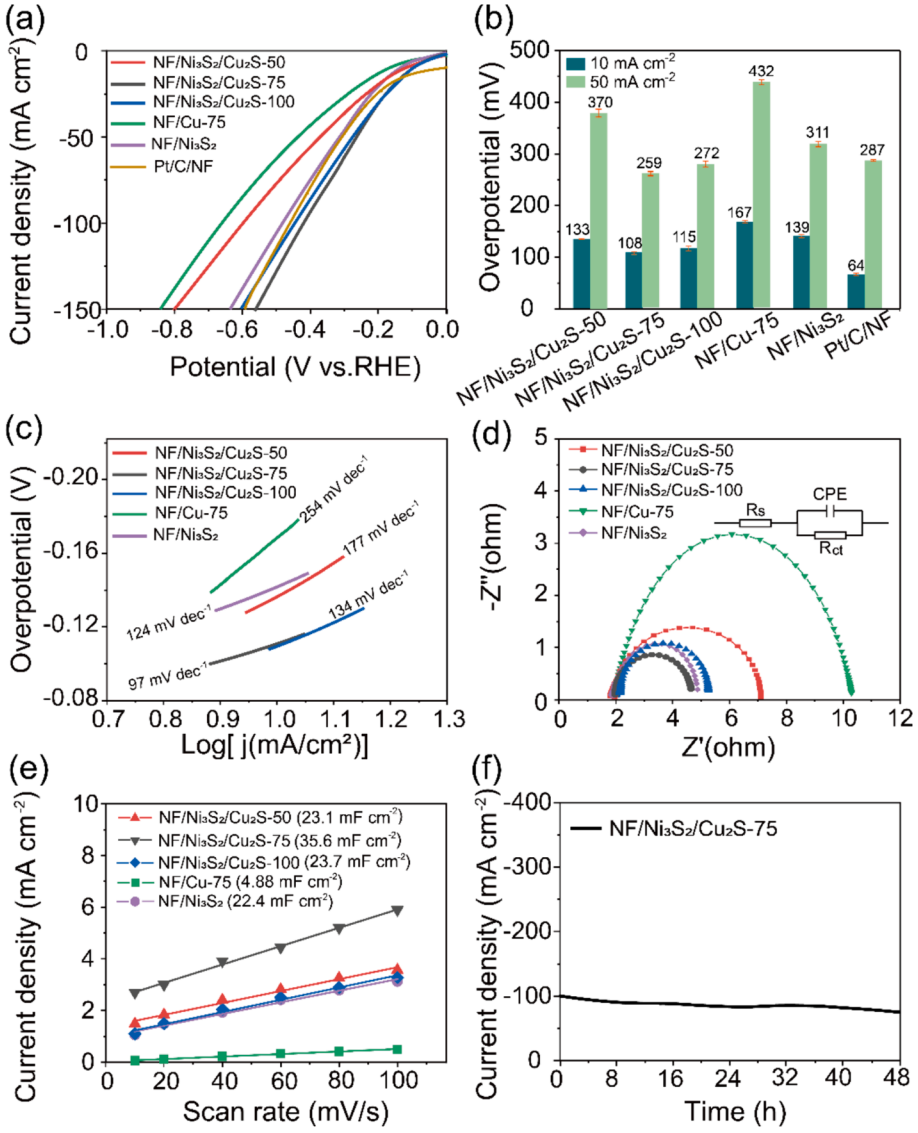

Fig. 7. HER performance of NF/Ni_3S_2/Cu_2S-X, NF/Cu-75, NF/Ni_3S_2, and Pt/C/NF in 1 M KOH. (a) LSV curves of all samples (no iR correction). (b) Overpotentials of all samples at 10 and 50 mA cm^{-2}. The measured data were obtained at least after three times experiments. (c) Tafel plots of NF/Ni_3S_2/Cu_2S-X, NF/Cu-75, and NF/Ni_3S_2. (d) Nyquist plots of NF/Ni_3S_2/Cu_2S-X, NF/Cu-75, and NF/Ni_3S_2. (e) Double-layer capacitance of NF/Ni_3S_2/Cu_2S-X, NF/Cu-75, and NF/Ni_3S_2. (f) Chronoamperometric curve of NF/Ni_3S_2/Cu_2S-75 at a constant applied potential of −0.45 V *vs* RHE.

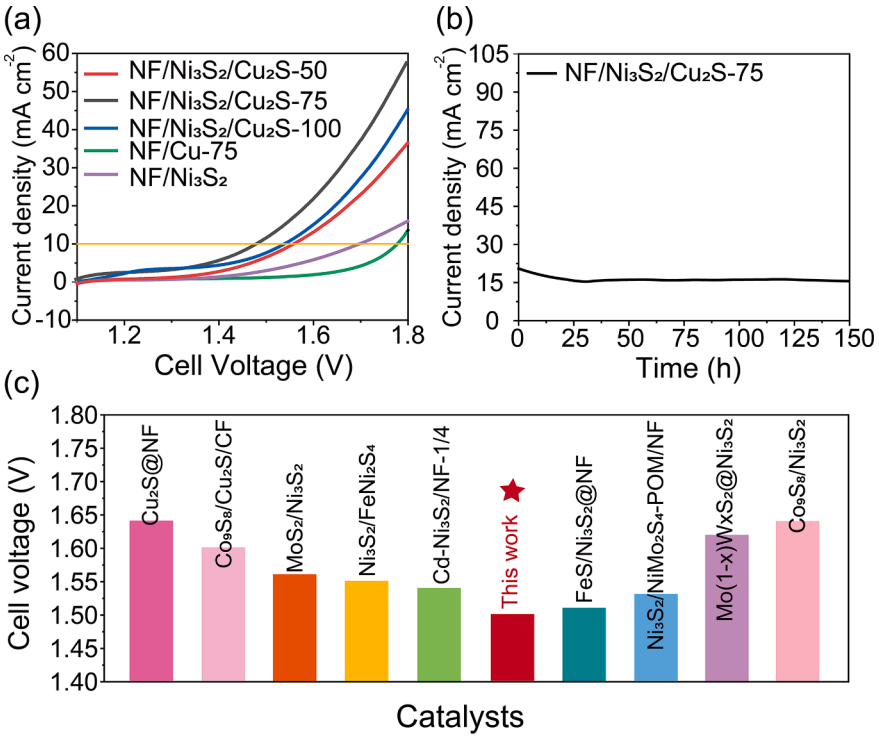

Fig. 8. Overall water splitting performance of NF/Ni_3S_2/Cu_2S-X, NF/Cu-75, and NF/Ni_3S_2 in 1 M KOH. (a) LSV curves of the cells with different electrodes for water electrolysis at a scan rate of 5 mV/s. (b) Chronoamperometric curve of NF/Ni_3S_2/Cu_2S-75 at a constant applied potential of 1.56 V. (c) Comparison of cell voltages between NF/Ni_3S_2/Cu_2S-75 and other reported catalysts at 10 mA cm^{-2}.

overpotentials at the 10 and 50 mA cm^{-2}. Moreover, the HER activity of NF/Ni_3S_2/Cu_2S-75 was superior to or comparable to that of most Cu_2S- and/or Ni_3S_2-based materials (Table 1) [18,20,23,28,58–65]. As evident from Table 1, many Cu_2S-based catalysts, such as Cu_2S@NF (η_{10} = 105 mV) [61], Co_9S_8/Cu_2S/CF (η_{10} = 165 mV) [20], and Cu_2S NRs@CoS/CF (η_{10} = 136 mV) [59], exhibited high HER activity. Meanwhile, Ni_3S_2-based materials, such as Cd-Ni_3S_2/NF (η_{10} = 140 mV) [23], FeS/Ni_3S_2@NF (η_{10} = 130 mV) [65], and Ni_3S_2/$FeNi_2S_4$ (η_{10} = 130 mV) [28], also exhibit acceptable HER performance. Owing to the high HER activities of both Cu_2S and Ni_3S_2, the construction of the NF/Ni_3S_2/Cu_2S heterojunction enhanced HER performance even further.

As shown in Fig. 7c, NF/Ni_3S_2/Cu_2S-75 exhibited the smallest Tafel slope (97 mV dec^{-1}) compared with NF/Ni_3S_2/Cu_2S-50 (177 mV dec^{-1}), NF/Ni_3S_2/Cu_2S-100 (134 mV dec^{-1}), NF/Cu-75 (254 mV dec^{-1}), and NF/Ni_3S_2 (124 mV dec^{-1}). This indicates that NF/Ni_3S_2/Cu_2S-75 exhibited faster HER kinetics. EIS was used to study the electrode reaction kinetics and charge transfer during HER. The Nyquist diagrams and specific data are shown in Fig. 7d and Table S4, respectively. NF/Ni_3S_2/Cu_2S-75 exhibited a significantly smaller semicircular radius (2.8 Ω) than other electrocatalysts, indicating improved charge-transfer kinetics in NF/Ni_3S_2/Cu_2S-75.

The electrochemically active surface area (ECSA) is proportional to the double-layer capacitance (C_{dl}). Therefore, the ECSA were calculated by determining the C_{dl} (Fig. 7e) from cyclic voltammetry (CV) (Fig. S4) tests conducted at scan rates from 10 to 100 mV s^{-1}. The calculated C_{dl} decreased in the order of NF/Ni_3S_2/Cu_2S-75 (35.6 mF cm^{-2}) > NF/Ni_3S_2/Cu_2S-100 (23.7 mF cm^{-2}) > NF/Ni_3S_2/Cu_2S-50 (23.1 mF cm^{-2}) > NF/Ni_3S_2 (22.4 mF cm^{-2}) > NF/Cu-75 (4.88 mF cm^{-2}). This suggests that the microspherical morphology and Ni_3S_2–Cu_2S interfaces endowed NF/Ni_3S_2/Cu_2S-75 with the highest number of electrochemically active sites. As shown in Fig. 7f, NF/Ni_3S_2/Cu_2S-75 catalyzed the HER at −100 mA cm^{-2} for up to 48 h without any obvious changes, demonstrating its excellent stability.

3.5. Overall water splitting

Because of its superior OER and HER performance, a two-electrode system with NF/Ni_3S_2/Cu_2S-75 as both the anode and cathode was built to study its overall water-splitting performance. As shown in Fig. 8a, at a current density of 10 mA cm^{-2}, the NF/Ni_3S_2/Cu_2S-75 exhibited a low cell voltage of 1.50 V, which was significantly lower than that of NF/Ni_3S_2/Cu_2S-50 (1.55 V), NF/Ni_3S_2/Cu_2S-100 (1.54 V), NF/Cu-75 (1.78 V), and NF/Ni_3S_2 (1.70 V). Moreover, NF/Ni_3S_2/Cu_2S-75 exhibited superior overall water-splitting performance compared with several previously reported Cu_2S- and/or Ni_3S_2-based materials, such as Cu_2S@NF (1.64 V) [61], Co_9S_8/Cu_2S/CF (1.6 V) [20], Cd-Ni_3S_2/NF (1.54 V) [23], MoS_2/Ni_3S_2 (1.56 V) [62], and $Mo_{(1-x)}W_xS_2$@Ni_3S_2 (1.62 V) [64]. Fig. 8c and Table 1 present a detailed comparison of the cell voltages of the materials. In addition, the NF/Ni_3S_2/Cu_2S-75 catalyst demonstrated satisfactory stability up to 150 h at 15 mA cm^{-2} (see Fig. 8b), which was far superior to those of Cu_2S@NF (20 h) [61] and many Ni_3S_2-based materials such as MoS_2/Ni_3S_2 (10 h) [62], Ni_3S_2/$NiMo_2S_4$-POM/NF (20 h) [63], and FeS/Ni_3S_2@NF (50 h) [65]. This indicates that the Ni_3S_2–Cu_2S heterojunction significantly improve the stability of NF/Ni_3S_2/Cu_2S-75 in water splitting, making it a promising candidate for large-scale hydrogen production.

The outstanding electrocatalytic performance of NF/Ni_3S_2/Cu_2S-75 can be attributed to the several factors. First, the in-situ growth of Ni_3S_2/Cu_2S on NF enhanced adhesion, thus accelerating charge transfer and gas release. Second, the microspherical morphology of NF/Ni_3S_2/Cu_2S provided a large specific surface area and abundant catalytically active sites, thereby facilitating gas release. Finally, the synergistic effect between the Ni_3S_2 and Cu_2S heterogeneous interfaces promoted the electrochemical activity of NF/Ni_3S_2/Cu_2S-75.

3.6. Characterization of the samples after stability testing

XRD, SEM, and XPS measurements were performed to examine the morphology, composition, and electronic states after stability testing.

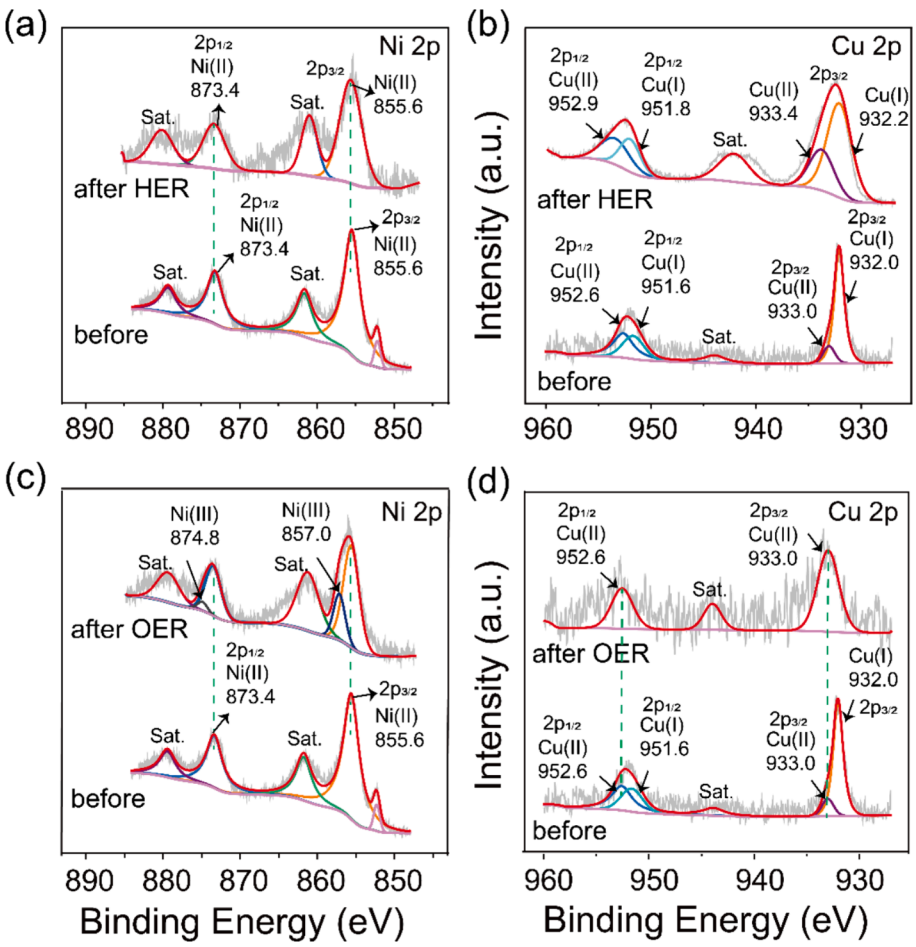

Fig. 9. XPS spectra of the samples before and after NF/Ni_3S_2/Cu_2S-75 underwent 150 h water splitting: (a) Ni 2p and (b) Cu 2p in cathode (HER); (c) Ni 2p and (d) Cu 2p in anode (OER).

Fig. S5A shows the XRD patterns with the main diffraction peaks of Ni_3S_2 and NF in the samples before and after 150 h of electrolysis. At the anode (OER), most of the Cu_2S was oxidized to CuO (JCPDS No. 48–1548) because of its oxidation potential. At the cathode (HER), Cu_2S transformed into Cu_2O (JCPDS No. 75–1531), with the +1 valence of Cu unchanged and only O replacing S. The SEM images (Fig. S5B) show that the catalysts in the cathode and anode maintained the microspherical morphology without much variation after 150 h of electrolysis.

The XPS spectra revealed slight changes in the Ni 2p and Cu 2p states (Fig. 9a and b) after the HER. After the OER, the peaks at 857.0 and 874.8 eV (Fig. 9c) corresponding to Ni $2p_{3/2}$ and Ni $2p_{1/2}$ states of Ni^{3+} [69] indicate partial oxidization of Ni^{2+} to Ni^{3+}. Furthermore, Fig. 9d shows that after the OER, most of the Cu^{+} ions were oxidized to Cu^{2+}, which is consistent with the CuO formation detected by XRD. Here, we consider the type of metal ion (either Cu^{+} or Cu^{2+}) that participates in the electrocatalytic process. Zuo et al. reported [38] that during in situ oxidation of Cu_2S to CuO, Cu_2S required an η_{10} of 286 mV for OER, whereas the Cu_2S-derived CuO required a higher η_{10} of 338 mV. This suggests that the Cu_2S exhibited better electrocatalytic performance than CuO. Moreover, the η_{10} value of Cu_2S (268 mV) [17] was significantly lower than that of CuS (408 mV) [70] toward OER. Thus, we conclude that a larger Cu^{+}/Cu^{2+} ratio corresponds to a higher electrocatalytic activity.

3.7. DFT calculations

The Ni_3S_2/Cu_2S interfacial interactions and their effect on the HER and OER activities were studied by DFT calculations. Based on the XRD results, Cu_2S (JCPDS No. 26–1116) possessed a hexagonal crystal lattice with the *P*63/*mmc* space group, whereas Ni_3S_2 (JCPDF No. 44–1418) possessed a trigonal crystal system with the *R*32 space group. The heterojunction was feasible for two reasons: first, the trigonal crystal system and hexagonal crystal system possessed similar cell parameters ($\alpha = \beta = 90°$, $\gamma = 120°$, $a = b \neq c$); second, the expansion of the $3 \times 3 \times 1$ Ni_3S_2 and $4 \times 4 \times 1$ Cu_2S cells reached more than 95% lattice matching. The optimized Cu_2S and Ni_3S_2/Cu_2S models are shown in Fig. 10A-a and b. The Cu_2S cell alone had poor stability, and its structure was distorted after structural optimization (Fig. S6). Interestingly, after constructing a heterojunction with Ni_3S_2, the Cu_2S stability significantly improved.

The total density of states (TDOS) of Cu_2S and Ni_3S_2/Cu_2S are shown in Fig. 10B and C, respectively. At the Fermi level, the DOS of single-phase Cu_2S was nearly zero, indicating that Cu_2S has semiconducting properties. In contrast, for the Ni_3S_2/Cu_2S heterojunction, the DOS at the Fermi level had a significantly high value of 60.03, demonstrating its higher carrier density at the Fermi level and good metallic character. This also indicated that the Ni_3S_2/Cu_2S heterojunction enhanced the intrinsic conductivity of Cu_2S.

For the partial density of states (PDOS), the contribution of an orbital to each atom is usually expressed as an area ratio [11]. For Cu_2S, the main contributing orbitals were the *d* orbitals of Cu and the *p* orbitals of S (Fig. 10D1 and D2). For Ni_3S_2/Cu_2S, the *d* orbitals of Cu and Ni and *p* orbitals of S were the main contributors to the TDOS (Fig. 10E1–E3).

Because ΔG_{H^*} is strongly correlated with the electrocatalytic activity in HER, we calculated the ΔG_{H^*} values for Cu_2S and the Ni_3S_2/Cu_2S heterostructure. Based on the optimized structures for hydrogen adsorption on the Cu and S sites of Cu_2S (Fig. S7), the $|\Delta G_{H^*}|$ was 5.76

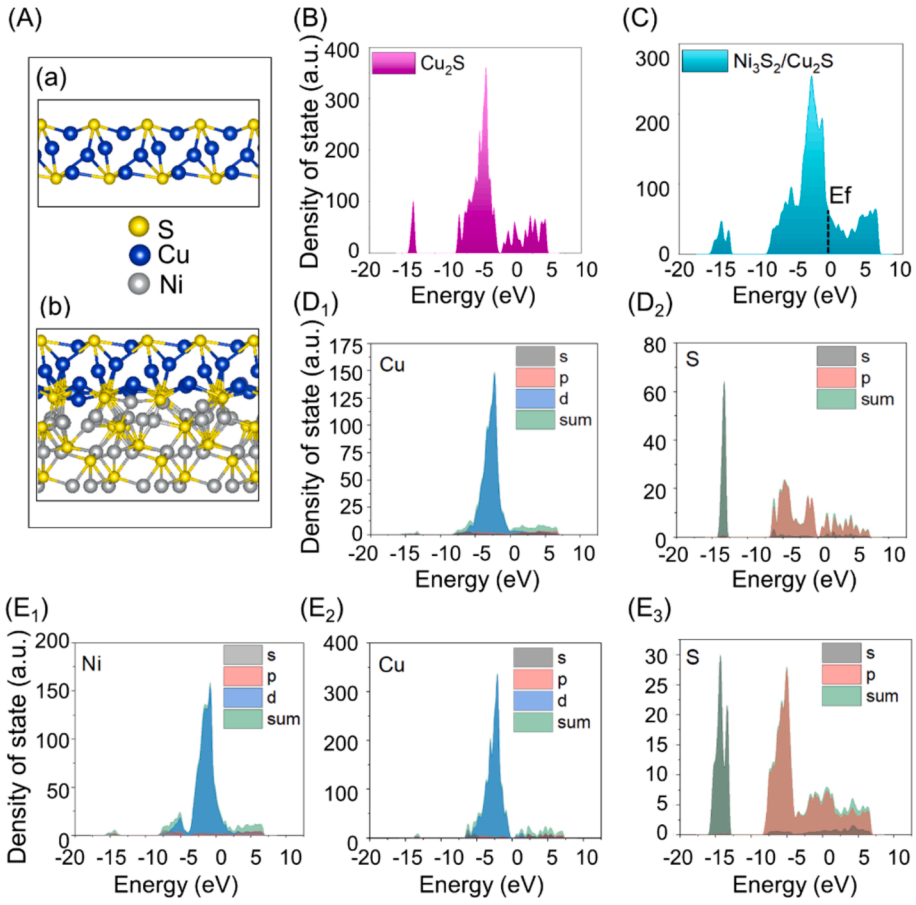

Fig. 10. (A) From side view, structure optimization diagram of (a) Cu_2S and (b) Ni_3S_2/Cu_2S (blue, yellow, and grey spheres indicate Cu, S, and Ni atoms, respectively); Calculated TDOS of (B) Cu_2S and (C) Ni_3S_2/Cu_2S, and PDOS of (D_1) Cu and (D_2) S of Cu_2S and (E_1) Ni, (E_2) Cu, (E_3) S of Ni_3S_2/Cu_2S. (For interpretation of the references to color in this figure legend, the reader is referred to the web version of this article.)

eV at the Cu site and 5.09 eV at the S site. The lower $|\Delta G_{H^*}|$ of S site indicates its potential as the HER active site. In addition, H* atoms were preferentially adsorbed on the S atoms in both Cu_2S and Ni_3S_2/Cu_2S (Fig. 11A), indicating that the active site was always S. As shown in Fig. 11B, the ΔG_{H^*} of Cu_2S was −5.09 eV, whereas the ΔG_{H^*} of heterojunction was −3.22 eV. The significant reduction in $|\Delta G_{H^*}|$ suggests that the Ni_3S_2/Cu_2S heterojunction facilitates a higher HER activity [71]. The negative ΔG_{H^*} implies that the H adsorption on the catalyst occurred easily, whereas hydrogen desorption was difficult, making desorption the rate-determining step (RDS) [72].

The charge transfer between H and S at the surfaces of Cu_2S (Fig. 11C-c1) and Ni_3S_2/Cu_2S (Fig. 11C-c2) was analyzed based on the charge density difference. The cyan part indicates a reduction in the charge density, whereas the yellow part indicates an increase. The loss of electrons from H and the accumulation of electrons on S show that electrons were transferred from H to S on both the Cu_2S and Ni_3S_2/Cu_2S surfaces. Compared with Cu_2S (Fig. 11 C-c_1), the reduced electron cloud density of H* on the Ni_3S_2/Cu_2S surface (Fig. 11 C-c_2) facilitated H* desorption, which is crucial for obtaining favorable ΔG_{H^*}. In addition, the electron gain and loss can be quantitatively analyzed using the plane-averaged charge density difference in the Z-direction [73], as shown in Fig. 11D. The positive and negative peaks correspond to electron gain and loss, respectively [74]. The S—H interfacial peak differences ($\Delta\rho$) for Ni_3S_2/Cu_2S were 0.3628 and –0.07455 e/Å (Fig. 11D-d2), which were significantly smaller than those for Cu_2S (1.3348 and –0.18473 e/Å; Fig. 11D-d1). This decrease in the electron cloud density of S—H on the Ni_3S_2/Cu_2S surface indicates the weakened S—H bond, which agrees with the reduced $|\Delta G_{H^*}|$ and favors improved HER activity.

The optimized ball-and-stick models of Cu_2S and Ni_3S_2/Cu_2S slabs and those for those for adsorption of *OH, *O, and *OOH during the OER are shown in Figs. S8 and S9, respectively. We found that the intermediates were always adsorbed on Cu, and the Cu atom tended to approach the surface of the material. The Gibbs free energy step diagrams for Ni_3S_2/Cu_2S are shown in Fig. S10. The red line indicates the maximum Gibbs free energy barrier, which indicates that the third step—formation of *OOH from *O—is the RDS, with an energy barrier of 2.50 eV.

Because XRD (Fig. 5A) patterns reveal that most Cu_2S was transformed to the CuO after the OER (JCPDS: 48–1548), whereas the Ni_3S_2 phase remained well-preserved, we constructed a heterojunction model of Ni_3S_2/CuO (Fig. S11) to further perform DFT calculations. Notably, we observed that intermediates (*OH, *O, and *OOH) were adsorbed on the Cu sites, indicating that Cu still functioned as the active site. As depicted in Fig. S12, the RDS of Ni_3S_2/CuO remained the third step (*O → *OOH), with a maximum Gibbs free energy barrier of 2.59 eV. Compared with Fig. S10 results, it is evident that despite the oxidation of Cu_2S to CuO, the active sites and RDS in the OER remained unchanged, and the lower Gibbs free energy barrier of Ni_3S_2/Cu_2S heterojunction model demonstrated better OER performance. To conclude, the pristine heterojunction of Ni_3S_2/Cu_2S was rationally designed and the Cu^+ (in Cu_2S) showed better electrocatalytic performance than Cu^{2+} (in CuO).

Based on the abovementioned results, the excellent overall water splitting performance of Ni_3S_2/Cu_2S was attributed to the following reasons: (1) the unique microspherical morphology of Ni_3S_2/Cu_2S endowed it with a large specific surface area and numerous active sites; (2) NF not only served as a substrate but also as an Ni source to construct the Ni_3S_2/Cu_2S heterojunction, thus improving the catalyst stability; (3)

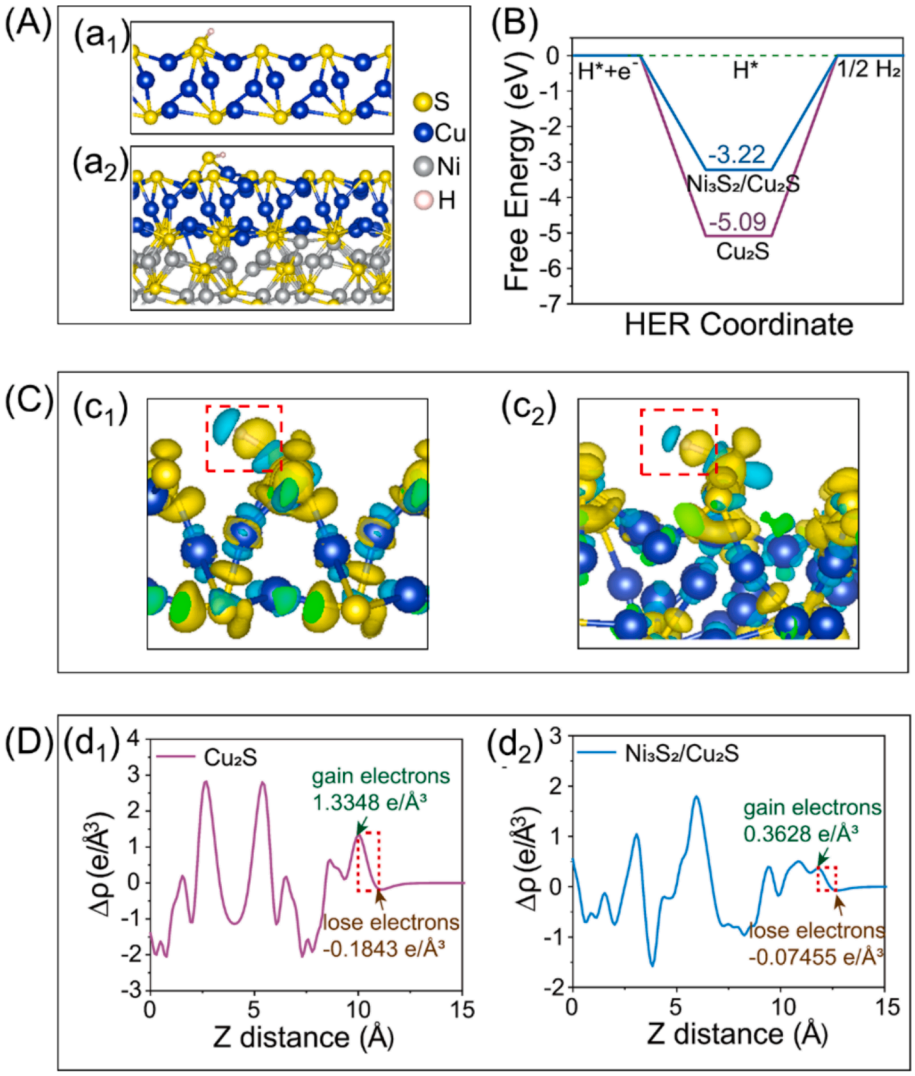

Fig. 11. (A) Optimized structural model of H adsorption on (a_1) Cu_2S and (a_2) Ni_3S_2/Cu_2S. White, blue, yellow, and grey spheres indicate H, Cu, S, and Ni, respectively. (B) Gibbs free-energy diagram of HER on Cu_2S and Ni_3S_2/Cu_2S at U=0 V. (C) Charge differential density diagram of (c_1) Cu_2S and (c_2) Ni_3S_2/Cu_2S. White, blue, and yellow spheres indicate H, Cu, and S atoms, respectively. The cyan part indicates a decrease in charge density, and yellow part indicates an increase in charge density. (D) Plane-averaged charge density difference (Δρ) along Z-direction normal to the side views of (d_1) Cu_2S and (d_2) Ni_3S_2/Cu_2S. (For interpretation of the references to color in this figure legend, the reader is referred to the web version of this article.)

the Ni_3S_2/Cu_2S possessed a higher carrier density at the Fermi level, which enhanced the intrinsic conductivity of the catalyst; (4) the decreased electron cloud density of S—H on the Ni_3S_2/Cu_2S surface weakened the S—H bond, thereby reducing $|\Delta G_{H^*}|$ and improving HER catalytic activity.

4. Conclusion

A Ni_3S_2/Cu_2S heterojunction with a unique microspherical morphology was grown in situ on nickel foam (NF) via an electrodeposition–hydrothermal method. Compared with previous studies that reported Cu_2S-based electrocatalysts on Cu foam (CF) [15,20], this study involved electrodepositing a uniform layer of metallic Cu^0 on the NF substrate, with subsequent vulcanization producing more compact bimetallic sulfides with higher stability. The interfacial effect between Ni_3S_2 and Cu_2S significantly enhanced the electron transfer, improving the water-splitting performance. Density functional theory (DFT) calculations demonstrated that Ni_3S_2/Cu_2S exhibited higher activity than Cu_2S alone, and its higher density of state (DOS) at the Fermi level led to better metallic character. The negative Gibbs free energy of hydrogen adsorption (ΔG_{H^*}) implied that hydrogen desorption was the rate-determining step during HER. The calculated charge differential density showed that the interfacial effect of Ni_3S_2/Cu_2S weakened S—H bonding, which facilitated hydrogen desorption, thereby accelerating H_2 generation. This study presents a novel approach for tailoring cost-efficient sulfide-based electrocatalysts for overall water splitting to produce hydrogen.

CRediT authorship contribution statement

Siqi Zhang: Writing – review & editing, Writing – original draft, Methodology, Investigation, Conceptualization. **Huiqin Yao:** Project administration, Funding acquisition, Conceptualization. **Ruxin Deng:** Methodology, Investigation. **Jiayi Zhan:** Methodology, Investigation. **Tian Tong:** Validation, Methodology, Investigation. **Yixuan Wang:** Formal analysis, Data curation. **Haiqing Yan:** Validation, Investigation. **Chaonan Wang:** Validation, Methodology, Investigation. **Cheng Li:** Validation, Project administration, Methodology. **Hongliang Dong:** Validation, Methodology, Investigation. **Shulan Ma:** Writing – review & editing, Supervision, Funding acquisition, Conceptualization.

Declaration of competing interest

The authors declare that they have no known competing financial interests or personal relationships that could have appeared to influence the work reported in this paper.

Data availability

Data will be made available on request.

Acknowledgements

This work is supported by the National Science Foundation of China (No. 22176017), Natural Science Foundation of Ningxia (2023AAC02039), Shanghai Key Laboratory of Material Frontiers Research in Extreme Environments (MFree), China (No. 22dz2260800), and Shanghai Science and Technology Committee, China (No. 22JC1410300). We also thank the 1W2B beamline station at Beijing Synchrotron Radiation Facility (BSRF), the BL17B station of National Facility for Protein Science in Shanghai (NFPS) and BL13SSW station at Shanghai Synchrotron Radiation Facility (SSRF) for the help in characterizations.

Appendix A. Supplementary data

Supplementary data to this article can be found online at https://doi.org/10.1016/j.jcis.2024.09.110.

References

[1] C. Zhang, H. Wang, H. Yu, K. Yi, W. Zhang, X. Yuan, J. Huang, Y. Deng, G. Zeng, Single-atom catalysts for hydrogen generation: Rational design, recent advances, and perspectives, Adv. Energy Mater. 12 (2022) 2200875.
[2] C. Zhang, Y. Deng, Q. Wan, H. Zeng, H. Wang, H. Yu, H. Pang, W. Zhang, X. Yuan, J. Huang, Built-in electric field boosted exciton dissociation in sulfur doped BiOCl with abundant oxygen vacancies for transforming the pathway of molecular oxygen activation, Appl. Catal. b: Environ. 343 (2024) 123557.
[3] B. Zhou, R. Gao, J.J. Zou, H. Yang, Surface design strategy of catalysts for water electrolysis, Small 18 (2022) 2202336.
[4] F. Wang, P. Zou, Y. Zhang, W. Pan, Y. Li, L. Liang, C. Chen, H. Liu, S. Zheng, Activating lattice oxygen in high-entropy LDH for robust and durable water oxidation, Nat. Commun. 14 (2023) 6019.
[5] Y. Wang, X. Lei, B. Zhang, B. Bai, P. Das, T. Azam, J. Xiao, Z.S. Wu, Breaking the Ru−O−Ru symmetry of a RuO_2 catalyst for sustainable acidic water oxidation, Angew. Chem. Int. Edit. 63 (2023) e202316903.
[6] Y. Zhao, J. You, L. Wang, W. Bao, R. Yao, Recent advances in Ni_3S_2-based electrocatalysts for oxygen evolution reaction, Int. J. Hydrogen Energ. 46 (2021) 39146–39182.
[7] C. Wang, P. Zhai, M. Xia, W. Liu, J. Gao, L. Sun, J. Hou, Identification of the origin for reconstructed active sites on oxyhydroxide for oxygen evolution reaction, Adv. Mater. 35 (2022) 2209307.
[8] Y. Chen, L. Wang, W. Wang, M. Cao, Enhanced photoelectrochemical properties of ZnO/ZnSe/CdSe/Cu_{2-x}Se core–shell nanowire arrays fabricated by ion-replacement method, Appl. Catal. b: Environ. 209 (2017) 110–117.
[9] R. Yang, Y. Zhou, Y. Xing, D. Li, D. Jiang, M. Chen, W. Shi, S. Yuan, Synergistic coupling of CoFe-LDH arrays with NiFe-LDH nanosheet for highly efficient overall water splitting in alkaline media, Appl. Catal. b: Environ. 253 (2019) 131–139.
[10] T.T. Liu, Y.C. Wang, Y.Z. Wang, M.S. Cao, "Heterodimensional Structure" integrated defect and interface engineering for efficiently EMI shielding and electrochemical response, Adv. Funct. Mater. 2404280 (2024).
[11] R. Deng, H. Yao, Y. Wang, C. Wang, S. Zhang, S. Guo, Y. Li, S. Ma, Interface effect of Fe doped NiSe/Ni_3Se_2 heterojunction as highly efficient electrocatalysts for overall water splitting, Chem. Eng. J. 488 (2024) 150996.
[12] M. Wang, L. Zhang, Y. He, H. Zhu, Recent advances in transition-metal-sulfide-based bifunctional electrocatalysts for overall water splitting, J. Mater. Chem. A 9 (2021) 5320–5363.
[13] J. Jiang, H. Su, S. Song, W. Liu, N. Li, Y. Gao, L. Ge, W-doped $FeNi_2S_4$/Ni_3S_2/NF with interfacial effect as efficient bifunctional electrocatalyst for overall water splitting, Nano Res. 16 (2023) 12116–12125.
[14] N. Zhang, S. Huang, L. Chen, Y. Li, M. Tang, Q. Pei, J. Liu, Superhydrophilic/superaerophobic amorphous Ni_3S_2/NiMoS electrocatalyst for enhanced hydrogen evolution, J. Colloid Interf. Sci. 652 (2023) 95–103.
[15] Y. Hu, J. Zhu, H. Yang, S. Lyu, J. Chen, Anti-corrosion engineering of Cu_2S/FeOOH hybrid nanosheets as superior bifunctional electrocatalysts for overall water splitting, Inorg. Chem. Commun. 117 (2020) 107971.
[16] Y. Pei, J. Cheng, H. Zhong, Z. Pi, Y. Zhao, F. Jin, Sulfide-oxidation-assisted electrochemical water splitting for H_2 production on a bifunctional Cu_2S/nickel foam catalyst, Green Chem. 23 (2021) 6975–6983.
[17] T. Marimuthu, R. Yuvakkumar, G. Ravi, Y. Zheng, Z. Bi, X. Xu, G. Xu, D. Velauthapillai, One-step fabrication of copper sulfide catalysts for HER in natural seawater and their bifunctional properties in freshwater splitting, Fuel 322 (2022) 124073.
[18] K.S. Bhat, H.S. Nagaraja, In situ synthesis of copper sulfide-nickel sulfide arrays on three-dimensional nickel foam for overall water splitting, ChemistrySelect 5 (2020) 2455–2464.
[19] M. Tang, Y. Liu, H. Cao, Q. Zheng, X. Wei, K.H. Lam, D. Lin, Cu_2S/Ni_3S_2 ultrathin nanosheets on Ni foam as a highly efficient electrocatalyst for oxygen evolution reaction, Int. J. Hydrogen Energ. 47 (2022) 3013–3021.
[20] Z. Zang, X. Wang, X. Li, Q. Zhao, L. Li, X. Yang, X. Yu, X. Zhang, Z. Lu, Co_9S_8 nanosheet coupled Cu_2S nanorod heterostructure as efficient catalyst for overall water splitting, ACS Appl. Mater. & Interfaces 13 (2021) 9865–9874.
[21] M. Zhong, W. Li, J. Chen, S. Ren, R. Qi, C. Wang, X. Lu, Surface reconstruction of Fe (III)/NiS nanotubes for generating high-performance oxygen-evolution catalyst, Sep. Purif. Technol. 310 (2023) 123164.
[22] F. Liu, X. Zhang, H. Zong, H. Xu, J. Xu, J. Liu, Facile construction Co-doped and CeO_2 heterostructure modified NiS_2 grown on foamed nickel for high-performance bifunctional water electrolysis catalysts, Int. J. Hydrogen Energ. 51 (2024) 314–322.
[23] H. Yan, R. Deng, S. Zhang, H. Yao, J. Duan, H. Bai, Y. Li, R. Liu, K. Shi, S. Ma, Cd doped Ni_3S_2 nanosheet arrays grown on nickel foam as highly efficient and robust bifunctional electrocatalysts for alkaline overall water splitting, J. Alloy. Compd. 954 (2023) 170072.
[24] K. Wan, J. Luo, C. Zhou, T. Zhang, J. Arbiol, X. Lu, B.W. Mao, X. Zhang, J. Fransaer, Hierarchical porous Ni_3S_4 with enriched high-valence Ni sites as a robust electrocatalyst for efficient oxygen evolution reaction, Adv. Funct. Mater. 29 (2019) 1900315.
[25] G. Zhao, Y. Xing, Y. Liu, X. Wang, B. Zhang, L. Mu, W. Liao, X. Xu, Built-in electric field in bifunctional electrocatalyst (Ni_3S_2@Ni_9S_8) for high-efficiency OER and overall water splitting performance, Mater. Today Chem. 34 (2023) 101758.
[26] Z. Yao, K. Yu, M. Pan, H. Xu, T. Zhao, Z. Jiang, A mechanically durable, excellent recyclable 3D hierarchical Ni_3S_2@Ni foam photothermal membrane, Green Energy & Environ. 7 (2022) 492–499.
[27] Y. Yang, K. Zhang, H. Lin, X. Li, H.C. Chan, L. Yang, Q. Gao, MoS_2–Ni_3S_2 heteronanorods as efficient and stable bifunctional electrocatalysts for overall water splitting, ACS Catal. 7 (2017) 2357–2366.
[28] Y. Wu, Y. Li, M. Yuan, H. Hao, X. San, Z. Lv, L. Xu, B. Wei, Operando capturing of surface self-reconstruction of Ni_3S_2/$FeNi_2S_4$ hybrid nanosheet array for overall water splitting, Chem. Eng. J. 427 (2022) 131944.
[29] M.-T. Chen, J.-J. Duan, J.-J. Feng, L.-P. Mei, Y. Jiao, L. Zhang, A.-J. Wang, Iron, rhodium-codoped Ni_2P nanosheets arrays supported on nickel foam as an efficient bifunctional electrocatalyst for overall water splitting, J. Colloid Interf. Sci. 605 (2022) 888–896.
[30] Z. Yu, H. Yao, Y. Yang, M. Yuan, C. Li, H. He, T.-S. Chan, D. Yan, S. Ma, P. Zapol, M. G. Kanatzidis, MoO_xS_y/Ni_3S_2 microspheres on Ni foam as highly efficient, durable electrocatalysts for hydrogen evolution reaction, Chem. Mater. 34 (2022) 798–808.
[31] Y. Yang, H. Yao, Z. Yu, S.M. Islam, H. He, M. Yuan, Y. Yue, K. Xu, W. Hao, G. Sun, H. Li, S. Ma, P. Zapol, M.G. Kanatzidis, Hierarchical nanoassembly of MoS_2/Co_9S_8/Ni_3S_2/Ni as a highly efficient electrocatalyst for overall water splitting in a wide pH range, J. Am. Chem. Soc. 141 (2019) 10417–10430.
[32] B. Qiao, H. Yan, C. Wang, H. Yao, Z. Cai, K. Shi, R. Liu, S. Ma, Ni_xS_y/NF composites assembled by sulfidation of nickel foam (NF) for highly effective capture of iodine, Chem. Eng. J. 479 (2024) 147864.
[33] R.C.A.J.J. Rehr, Theoretical approaches to x-ray absorption fine structure, Rev. Mod. Phys. 72 (2000) 621.
[34] G. Kresse, J. Hafner, Ab initiomolecular-dynamics simulation of the liquid-metal–amorphous-semiconductor transition in germanium, Phys. Rev. B 49 (1994) 14251–14269.
[35] M. Guo, M. Ji, W. Cui, Theoretical investigation of HER/OER/ORR catalytic activity of single atom-decorated graphyne by DFT and comparative DOS analyses, Appl. Surf. Sci. 592 (2022) 153237.
[36] K.-L. Yan, X. Shang, Z. Li, B. Dong, J.-Q. Chi, Y.-R. Liu, W.-K. Gao, Y.-M. Chai, C.-G. Liu, Facile synthesis of binary NiCoS nanorods supported on nickel foam as efficient electrocatalysts for oxygen evolution reaction, Int. J. Hydrogen Energ. 42 (2017) 17129–17135.
[37] H. Yan, R. Deng, C. Wang, H. Yao, S. Guo, R. Liu, S. Ma, Amorphous Fe hydroxide nanoparticles embedded in Ni_3S_2 as high-efficiency and low-cost electrocatalysts for oxygen evolution reaction, Electrochim. Acta 427 (2022) 140889.
[38] Y. Zuo, Y. Liu, J. Li, R. Du, X. Han, T. Zhang, J. Arbiol, N.J. Divins, J. Llorca, N. Guijarro, K. Sivula, A. Cabot, In situ electrochemical oxidation of Cu_2S into CuO nanowires as a durable and efficient electrocatalyst for oxygen evolution reaction, Chem. Mater. 31 (2019) 7732–7743.
[39] Q. Wang, J. Li, J. Li, Enhanced thermoelectric performance of Cu_3SbS_4 flower-like hierarchical architectures composed of Cl doped nanoflakes via an in situ generated CuS template, Phys. Chem. Chem. Phys. 20 (2018) 1460–1475.
[40] M. Sun, X. Guan, Q. huang, Q. Gao, S. Zhang, X. Cai, Y. Fang, F. Peng, S. Yang, CdS@Ni_3S_2/Cu_2S electrode for electrocatalysis and boosted photo-assisted electrocatalysis hydrogen production, Sep. Purif. Technol. 319 (2023) 124085.
[41] T. Bezghiche-Imloul, H. Hammache-Makhloufi, N. Ait Ahmed, Electrocatalytic oxidation of alcohols on Cu_2O/Cu thin film electrodeposited on titanium substrate, Surf. Rev. Lett. 23 (2016) 1650041.

[42] Q. Wu, Q. Gao, L. Sun, H. Guo, X. Tai, D. Li, L. Liu, C. Ling, X. Sun, Facilitating active species by decorating CeO_2 on Ni_3S_2 nanosheets for efficient water oxidation electrocatalysis, Chinese, J. Catal. 42 (2021) 482–489.
[43] N. Zhang, Y. Li, R. Zhang, S. Huang, F. Wang, M. Tang, J. Liu, Tiny Ni_3S_2 boosting MoS_2 hydrogen evolution in alkali by enlarging coupling boundaries and stimulating basal plane, J. Colloid Interf. Sci. 642 (2023) 479–487.
[44] S.B. Kale, P.T. Babar, J.-H. Kim, C.D. Lokhande, Synthesis of one dimensional Cu_2S nanorods using a self-grown sacrificial template for the electrocatalytic oxygen evolution reaction (OER), New J. Chem. 44 (2020) 8771–8777.
[45] Y. He, Y. Wang, X. Wang, R. Li, W. Lu, Fabrication of NiCo@Ni_3S_2/Nickel foam electrocatalyst with ultrathin NiCo layered double hydroxide film wrapping Ni_3S_2 nanoarrays for efficient oxygen evolution reaction, Int. J. Hydrogen Energ. 48 (2023) 35962–35970.
[46] F. Qiao, S. Qian, W. Liu, T. Zhou, J. Yang, J. Zhao, J. Yuan, Cu_2O/Cu_2S microstructure regulation towards high efficiency photocatalytic hydrogen production and its theoretical mechanism analysis, CrystEngComm 25 (2023) 4939–4945.
[47] I.-R. Jo, J.A. Rajesh, Y.-H. Lee, J.-H. Park, K.-S. Ahn, Enhanced electrocatalytic activity and electrochemical stability of Cu_2S/PbS counter electrode for quantum-dot-sensitized solar cells, Appl. Surf. Sci. 525 (2020) 146643.
[48] T.-W. Chen, U. Rajaji, S.-M. Chen, M. Govindasamy, S.S. Paul Selvin, S. Manavalan, R. Arumugam, Sonochemical synthesis of graphene oxide sheets supported Cu_2S nanodots for high sensitive electrochemical determination of caffeic acid in red wine and soft drinks, Compos. Part b: Eng. 158 (2019) 419–427.
[49] B. Pejjai, M. Reddivari, T.R.R. Kotte, Phase controllable synthesis of CuS nanoparticles by chemical co-precipitation method: Effect of copper precursors on the properties of CuS, Mater. Chem. Phys. 239 (2020) 122030.
[50] F. Si, C. Tang, Q. Gao, F. Peng, S. Zhang, Y. Fang, S. Yang, Bifunctional CdS@Co_9S_8/Ni_3S_2 catalyst for efficient electrocatalytic and photo-assisted electrocatalytic overall water splitting, J. Mater. Chem. A 8 (2020) 3083–3096.
[51] L. Wang, X. Xue, Q. Luan, J. Guo, L. Chu, Z. Wang, B. Li, M. Yang, G. Wang, Interface engineering of Mo-doped Ni_9S_8/Ni_3S_2 multiphase heterostructure nanoflowers by one step synthesis for efficient overall water splitting, Journal of Colloid Interf. Sci. 634 (2023) 563–574.
[52] Y. Wu, Y. Li, Z. Lü, L. Xu, B. Wei, Heterostructural Ni_3S_2–$Fe_5Ni_4S_8$ hybrids for efficient electrocatalytic oxygen evolution, J. Mater. Sci. 55 (2020) 15963–15974.
[53] T. Ohnuma, T. Kobayashi, X-ray absorption near edge structure simulation of $LiNi_{0.5}Co_{0.2}Mn_{0.3}O_2$ via first-principles calculation, RSC Adv. 9 (2019) 35655–35661.
[54] Y. Yang, Y. Xie, Z. Yu, S. Guo, M. Yuan, H. Yao, Z. Liang, Y.R. Lu, T.-S. Chan, C. Li, H. Dong, S. Ma, Self-supported NiFe-LDH@CoS_x nanosheet arrays grown on nickel foam as efficient bifunctional electrocatalysts for overall water splitting, Chem. Eng. J. 419 (2021) 129512.
[55] Y. Liu, H. Cheng, M. Lyu, S. Fan, Q. Liu, W. Zhang, Y. Zhi, C. Wang, C. Xiao, S. Wei, B. Ye, Y. Xie, Low overpotential in vacancy-rich ultrathin $CoSe_2$ nanosheets for water oxidation, J. Am. Chem. Soc. 136 (2014) 15670–15675.
[56] Y. Zhao, X. Jia, G. Chen, L. Shang, G.I.N. Waterhouse, L.-Z. Wu, C.-H. Tung, D. O'Hare, T. Zhang, Ultrafine NiO nanosheets stabilized by TiO_2 from monolayer NiTi-LDH precursors: An active water oxidation electrocatalyst, J. Am. Chem. Soc. 138 (2016) 6517–6524.
[57] Z. Wang, P. Guo, S. Cao, H. Chen, S. Zhou, H. Liu, H. Wang, J. Zhang, S. Liu, S. Wei, D. Sun, X. Lu, Contemporaneous inverse manipulation of the valence configuration to preferred Co^{2+} and Ni^{3+} for enhanced overall water electrocatalysis, Appl. Catal. b: Environ. 284 (2021) 119725.
[58] M.S. Hassan, P. Basera, S. Gahlawat, P.P. Ingole, S. Bhattacharya, S. Sapra, Understanding the efficient electrocatalytic activities of $MoSe_2$–Cu_2S nanoheterostructures, J. Mater. Chem. A 9 (2021) 9837–9848.
[59] Q. Zhou, T.-T. Li, J. Wang, F. Guo, Y.-Q. Zheng, Hierarchical Cu_2S NRs@CoS core-shell structure and its derivative towards synergistic electrocatalytic water splitting, Electrochim. Acta 296 (2019) 1035–1041.
[60] F. Du, L. Shi, Y. Zhang, T. Li, J. Wang, G. Wen, A. Alsaedi, T. Hayat, Y. Zhou, Z. Zou, Foam–like Co_9S_8/Ni_3S_2 heterostructure nanowire arrays for efficient bifunctional overall water–splitting, Appl. Catal. b: Environ. 253 (2019) 246–252.
[61] Z. Han, G. Li, X. Zeng, Y. Zhu, N. Li, J. Zhang, W. Zhao, Q. Jiao, Electrochemical construction of Cu@NF frameworks and synthesis of self-supported microflower Cu_2S@NF as bifunctional catalysts for overall water splitting, Int. J. Hydrogen Energ. 47 (2022) 15695–15705.
[62] J. Zhang, T. Wang, D. Pohl, B. Rellinghaus, R. Dong, S. Liu, X. Zhuang, X. Feng, Interface engineering of MoS_2/Ni_3S_2 heterostructures for highly enhanced electrochemical overall-water-splitting activity, Angew. Chem. Int. Edit. 55 (2016) 6702–6707.
[63] J. Fang, X. Qian, J. Xia, B. Huang, G. He, Z. Zhang, H. Chen, Heterostructure engineering of self-supported bimetallic sulfide as an efficient bifunctional electrocatalyst for overall water splitting, J. Alloy. Compd. 937 (2023) 168339.
[64] M. Zheng, J. Du, B. Hou, C.-L. Xu, Few-Layered $Mo_{(1-x)}W_xS_2$ hollow nanospheres on Ni_3S_2 nanorod heterostructure as robust electrocatalysts for overall water splitting, ACS Appl. Mater. & Interfaces 9 (2017) 26066–26076.
[65] H. Li, S. Yang, W. Wei, M. Zhang, Z. Jiang, Z. Yan, J. Xie, Chrysanthemum-like FeS/Ni_3S_2 heterostructure nanoarray as a robust bifunctional electrocatalyst for overall water splitting, J. Colloid Interf. Sci. 608 (2022) 536–548.
[66] K. Gothandapani, R.S. Jeniffer, G. Tamil Selvi, V. Velmurugan, A.K. Assaifan, K. E. Alzahrani, H. Albrithen, M. Muthuramamoorthy, S. Pandiaraj, S. Pitchaimuthu, A.N. Alodhayb, A.N. Grace, Nickel nanoparticles supported on carbon surface as an electrocatalyst for hydrogen evolution reaction, Int. J. Hydrogen Energ. 52 (2024) 1137–1146.
[67] R. Huang, Y. Wen, H. Peng, B. Zhang, Improved kinetics of OER on Ru-Pb binary electrocatalyst by decoupling proton-electron transfer, Chinese, J. Catal. 43 (2022) 130–138.
[68] Z. Wu, Y. Zhao, H. Wu, Y. Gao, Z. Chen, W. Jin, J. Wang, T. Ma, L. Wang, Corrosion engineering on iron foam toward efficiently electrocatalytic overall water splitting powered by sustainable energy, Adv. Funct. Mater. 31 (2021) 2010437.
[69] Y. Bu, Y. Zhang, Y. Liu, S. Li, Y. Zhou, X. Lin, Z. Dong, R. Zhang, J. Zhang, D. Zhang, MOF-derived urchin-like Co_9S_8-Ni_3S_2 composites on Ni foam as efficient self-supported electrocatalysts for oxygen evolution reaction, Batteries 9 (2023) 46.
[70] H. Liang, W. Shuang, Y. Zhang, S. Chao, H. Han, X. Wang, H. Zhang, L. Yang, Graphene-like multilayered CuS nanosheets assembled into flower-like microspheres and their electrocatalytic oxygen evolution properties, ChemElectroChem 5 (2017) 494–500.
[71] S. Dutta, S.K. Pati, Tetrazine Based covalent organic framework as a promising metal-free photo and electro-catalyst for HER, Catal. Lett. 152 (2022) 3548–3557.
[72] L. He, W. Zhang, Q. Mo, W. Huang, L. Yang, Q. Gao, Molybdenum carbide-oxide heterostructures: In situ surface reconfiguration toward efficient electrocatalytic hydrogen evolution, Angew. Chem. Int. Edit. 59 (2020) 3544–3548.
[73] Z. Xue, X. Zhang, J. Qin, R. Liu, Constructing MoS_2/g-C_3N_4 heterojunction with enhanced oxygen evolution reaction activity: A theoretical insight, Appl. Surf. Sci. 510 (2020) 145489.
[74] B. Qi, W. Chang, Q. Xu, L. Jiang, S. An, J.-F. Chu, Y.-F. Song, Regulating hollow carbon cage supported NiCo alloy nanoparticles for efficient electrocatalytic hydrogen evolution reaction, ACS Appl. Mater. & Interfaces 15 (2023) 12078–12087.